JOURNAL OF GEOPHYSICAL RESEARCH, VOL. 103, NO. E9, PAGES 20,089–20,112, AUGUST 30, 1998

JIM: A time-dependent, three-dimensional model of Jupiter's thermosphere and ionosphere

N. Achilleos, S. Miller, and J. Tennyson

Department of Physics and Astronomy, University College London, London, England

A. D. Aylward and I. Mueller-Wodarg

Atmospheric Physics Laboratory, University College London, London, England

D. Rees

Center for Atmospheric and Space Sciences, Utah State University, Logan

Abstract. We present the Jovian Ionospheric Model (JIM), a time-dependent, three-dimensional model for the thermosphere and ionosphere of Jupiter. We describe the physical inputs for the hydrodynamic, thermodynamic and chemical components of the model, which is based on the UCL Thermosphere Model of *Fuller-Rowell and Rees* [1980]. We then present the results of an illustrative simulation in which an initially neutral homogeneous planet evolves for approximately 4 Jovian rotations, under the influence of solar illumination and auroral (electron) precipitation at high latitudes. The model shows that solar zenith angle, auroral activity, ion recombination chemistry and, to a lesser degree, magnetic field orientation, all play a role in forming the dayside and nightside global ionization patterns. We compare auroral and nonauroral/equatorial ionospheric compositions and find the signature of ion transport by fast winds. We also include a localized "spot" of precipitation in our model and comment on the associated ionization signatures which develop in response to this Io-like aurora. The simulation also develops strong outflows with velocities up to $\sim$600 m s^{-1} from the auroral regions, driven mainly by pressure gradients. These pressure gradients, in turn, arise from the differences in chemical composition between the auroral and nonauroral upper thermospheres, as evolution proceeds. This preliminary study indicates a strong potential for JIM in analysis of two-dimensional image data and simulation of time-dependent global events.

1. Introduction

The physical coupling between the magnetosphere and ionosphere of Jupiter manifests itself as a wide variety of phenomena, observable at ultraviolet (UV) and infrared (IR) wavelengths, among others. In this important class are the following.

1. The dayglow, anomalously bright, global UV emission from excited H and H_2, is generally thought to arise from a combination of solar fluorescence and photoelectron impact [*Yelle*, 1988] with a possible additional energy source in the form of particle precipitation [*Shemansky*, 1985]. Recently, *Liu and Dalgarno* [1996] have been able to fit the UV spectrum of the dayglow with a model that employs solar fluorescence and photoelectron excitation without the need for an extra excitation source. On the other hand, *Waite et al.* [1997] and *Miller et al.* [1997], observing equatorial Xray emissions and low-latitude IR emission from H_3^+ ions, respectively, find that more energy is radiated in these wavelength regions than can be accounted for by only the relevant solar energy inputs.

2. The aurorae are high-latitude emissions resulting from the excitation and ionization of the upper atmosphere by energetic ($\geq$keV) charged particles precipitating, along magnetic field lines, from the magnetosphere.

Spectroscopy and two-dimensional (2-D) imaging of Jupiter's IR and UV auroral and global emissions, often interpreted through the use of appropriate models, sensitively probe the physical conditions in the Jovian ionosphere and magnetosphere, as well as the planet's magnetic field structure (recent examples include *Prangé and Elkhamsi* [1991], *Rego et al.* [1994], *Ballester et al.* [1996], *Baron et al.* [1996], *Lam et al.* [1997]). The IR emission from the molecular ion H_3^+, in particular, has become a well-established diagnostic of ionospheric tem-

Paper number 98JE00947.
0148-0227/98/98JE-00947$09.00

perature and density [e.g., *Ballester et al.,* 1994; *Lam et al.,* 1997] since its original detection on Jupiter a little under a decade ago [*Trafton et al.,* 1989; *Drossart et al.,* 1989].

Apart from ground-based observations of its emissions, more direct in situ observations of Jupiter's atmosphere and environs have been obtained by several space probes. Studies aimed at determining Jupiter's detailed ionospheric structure have all made use of at least one of the eight electron density (n_e) profiles deduced from the radio science (RSS) data of the Pioneer 10, Pioneer 11, Voyager 1, and Voyager 2 spacecraft [*Fjeldbo et al.,* 1975, 1976; *Eshleman et al.,* 1979a,b]. More recent determinations of ionospheric structure, using occultation data from the Galileo probe, have also been reported [*Hinson et al.,* 1997]. These entire data are currently the only available observational basis for such studies and have been the subject of many attempts to model the electron density in Jupiter's thermospheric region [e.g., *Atreya et al.,* 1979; *Waite et al.,* 1983; *McConnell and Majeed,* 1987; *Majeed and McConnell,* 1991]. In addition, the Voyager UVS data and, more recently, the measurements of the Galileo atmospheric probe have yielded information about Jupiter's thermospheric temperature profile. Subsequent comparison with theoretical temperature profiles has revealed the importance of various heating and cooling processes in maintaining the high temperatures (~1000 K) in the upper thermosphere [e.g., *Atreya et al.,* 1981; *Seiff et al.,* 1997].

The important results to emerge from these modeling studies have been the following.

1. The measured electron densities are generally lower (by about an order of magnitude) than those produced by 1-D models which include diffusion and chemistry. In addition, the measured peaks in n_e are situated at altitudes ~1000 km higher than the model peaks. However, the Galileo results [*Hinson et al.,* 1997] show a surprising variety of altitudes and densities at the main n_e peaks (there are complex layered structures near these peaks) which include those predicted by models.

2. The Jovian exospheric temperature is higher than that predicted by solar EUV heating alone (by a factor of ~2).

The system of thermospheric winds on Jupiter is regarded as a likely candidate for explaining the above discrepancies. These winds presumably flow outward from the auroral regions due to the high-energy inputs there. Inputs associated with both particle precipitation and Joule heating within the auroral regions have been previously estimated to be (each) of the order of 10 ergs cm^{-2} s^{-1}, in contrast with typical solar column heating rates of the order of 10^{-2} ergs cm^{-2} s^{-1} at the planet's equator [*Atreya,* 1986; *Prangé,* 1992 and references therein]. More recently, *Drossart et al.* [1993] have estimated the total IR auroral emission to be as high as 200 ergs cm^{-2} s^{-1}, which indicates even greater energy inputs associated with auroral precipitation and/or Joule heating. The bright localized UV aurora observed by *Gérard et al.* [1994] showed emission which was indicative of as much as 1000 ergs cm^{-2} s^{-1} of precipitation.

This wind system may transport some of the energy deposited in the auroral zones of Jupiter to the rest of the planet, and so provide the extra heating required to maintain the high thermospheric temperatures. In addition, the transport of ionospheric plasma by winds and electric fields could conceivably decrease the model electron densities and shift the n_e peak to higher altitudes. The potential role played by supersonic flows in such a process has been explored in the modeling study by *Sommeria et al.* [1995]. In addition, there have been studies which indicate that the upper thermospheric temperature profile may also be largely due to dissipation of energy by gravity waves and global precipitation of energetic ions [*Young et al.,* 1997; *Waite et al.,* 1997)].

In order to better assess global mechanisms of plasma and energy transport, it is necessary to extend 1-D thermospheric/ionospheric models to include two, or even three, dimensions and time dependence. This would enable, for example, computation of a global velocity distribution for thermospheric winds in a self-consistent manner. The efficiency of these winds as a means of transporting energy and charged species may then be explored using time-dependent simulations. Global models are also essential for more detailed analyses of 2-D images of Jupiter, which show characteristic emissions, at both auroral and nonauroral latitudes, dependent on latitude, longitude and local time [*Livengood et al.,* 1992; *Ballester et al.,* 1996; *Connerney et al.,* 1996; *Satoh et al.,* 1996; *Lam et al.,* 1997].

We present here the first time-dependent 3-D model of Jupiter's thermosphere and ionosphere (referred to as JIM, for Jovian Ionospheric Model). Clearly, a completely self-consistent model of this nature is an ambitious goal. In the case of JIM, the extension of all the computations involved in 1-D models to a 3-D grid has produced a model which yields useful and unique results, using standard computing facilities, within computational timescales that are still practical. The assumptions included in the model in order to facilitate computational expediency are described with the other input physics in section 2.

In section 3 we present results of a simulation which was evolved for 3.84 Jovian days (simulated time). We discuss mainly the global morphology of the H_3^+ and H^+ ionospheres, in terms of the reactions and transport processes which affect ion populations. We also present global distributions of the horizontal thermospheric winds, and constant-longitude cuts of neutral composition and temperature. Our goal in this paper is to provide a detailed description of the construction of JIM as well as its chemical, dynamic, and thermodynamic modeling capabilities. We emphasize therefore JIM's potential for future studies involving time-

dependent global physical events on Jupiter. Further simulations employed for comparison with appropriate observations have been described elsewhere [*Miller et al.*, 1997] and will be the subject of future studies.

2. The Model

Much of the numerical framework of JIM has been adapted from the UCL Thermosphere Model of *Fuller-Rowell and Rees* [1980]. This latter model simulates the time-dependent global winds, temperature, and composition of the neutral terrestrial thermosphere. This is achieved by numerically solving nonlinear equations of momentum, energy, and continuity. The UCL Thermosphere Model was, in 1983, fully coupled to a model of the terrestrial high-latitude ionosphere developed at Sheffield University [*Quegan et al.*, 1982, 1986]. This Coupled Thermosphere-Ionosphere Model (CTIM) [*Fuller-Rowell et al.*, 1996] has since been used in a large number of studies, such as the analysis of ground- and satellite-based measurements of wind velocity and neutral composition [e.g., *Rees and Fuller-Rowell*, 1989].

We use a similar numerical grid for our Jovian models to that used for the terrestrial models, namely, a spherical, corotating coordinate grid which divides the model planet into 40 elements in longitude (9° resolution), 91 elements in latitude (2° resolution), and 30 elements in pressure (which is used, instead of altitude, to define the vertical location of a grid cell). The vertical grid spacing is uniform with respect to the logarithm of pressure, so that the value of pressure for the nth layer may be written

$$P_n = P_1 \exp\{-\gamma(n-1)\} \tag{1}$$

We take $P_1 = 2$ μbar (at a constant altitude of 357 km above the 1 bar level) as our lower boundary and $\gamma = 0.4$ as the vertical spacing between levels in units of local pressure scale height. Our upper boundary is at pressure $P_{30} \approx 0.02$ nbar.

The horizontal wind velocity, ionospheric drift, total energy density, neutral composition, and ionospheric composition are evaluated at each grid point using explicit time stepping applied to finite difference versions of the appropriate equations of continuity, energy transport, and momentum transport (see sections 2.1, 2.2, and 2.6). Following *Fuller-Rowell* [1981], we use a time step satisfying a Courant condition and apply the double-smoothing filter of *Shapiro* [1970] to our numerical solutions in order to eliminate the spurious growth of Fourier components with wavelengths of two grid intervals and smaller. Using these solutions, the vertical wind, temperature, and altitudes at each pressure level can then be reevaluated after each step. We use a time step of 4 s in our calculations in order to adequately sample the minimum timescale ($\geq$10 s) associated with the recombination of H_3^+ ions in Jupiter's auroral ionosphere (section 2.5). The simulations described herein were computed on a Digital Alpha 500/500 workstation, for which one simulated rotation of the planet ($\sim$10 hours simulated time) required approximately 8 days of CPU time. We now describe the calculations in more detail.

2.1. Dynamics

Consider a Cartesian coordinate system situated at a particular grid point with the x, y, and z axes parallel to the local southward, eastward (here defined as the direction of decreasing System III longitude), and vertical directions, respectively. The horizontal momentum equation for the neutral gas may be written as follows :

$$\frac{D\boldsymbol{v}}{Dt} = -\frac{\nabla_z P}{\rho} + \boldsymbol{F} \tag{2}$$

where the left-hand term is the convective time derivative of the (2-D) horizontal velocity $\boldsymbol{v}$ and the right-hand terms are, first, the acceleration due to pressure gradients (here, ∇_z denotes the 2-D gradient operator acting in the x and y directions with z fixed) and, second, the extra acceleration due to the Coriolis force, viscosity effects, and neutral/ion collisions.

If we now transform to the P coordinate system [*Fuller-Rowell and Rees*, 1980], where pressure P rather than altitude z is used as a coordinate for locating any element of gas, the time derivative above can be expressed as follows :

$$\frac{D\boldsymbol{v}}{Dt} = \left(\frac{\partial \boldsymbol{v}}{\partial t}\right)_P + \boldsymbol{v}\cdot\nabla_P\boldsymbol{v} + w\frac{\partial \boldsymbol{v}}{\partial P} \tag{3}$$

where the center dot denotes scalar product and the subscript P denotes quantities evaluated at constant pressure. Again, ∇_P is a 2-D operator; $w = DP/Dt$ is the convective time derivative of pressure.

To cast the momentum equation, and those in the following sections, into forms appropriate for the P coordinate system, we require a relation between pressure and altitude. This is immediately provided in a simple form if we assume hydrostatic equilibrium in the vertical direction at each grid point. This assumption is valid provided that the timescale τ_{eq} for the reestablishment of hydrostatic equilibrium is small compared with the time scale τ_H for heating and temperature change. It is worth emphasizing this point.

Here $\tau_{eq} \sim (\Delta z/g)^{1/2}$, where Δz is the vertical extent of the thermosphere and g is the local acceleration due to gravity, is approximately the time scale for free-fall through a distance Δz. If we use $\Delta z = 2000$ km and $g = 25$ m s^{-2}, appropriate for Jupiter, then τ_{eq} is of the order of 5 min. Large horizontal velocities may effectively decrease g and increase τ_{eq} through the effect of the vertical component of the Coriolis force. This latter force is of the order of Ωu, where u is horizontal velocity and Ω is Jupiter's angular velocity. If we set $\Omega = 2 \times 10^{-4}$, we find that horizontal velocities $u \sim 12$ km s^{-1} will generate vertical Coriolis acceleration,

which is $\lesssim 0.1g$. Such velocities probably exist in the auroral thermosphere [*Sommeria et al.*,1995], which is a site of high-energy inputs. On the other hand, efficient heat conduction and transport (section 3.4) and the extremely efficient cooling of the auroral ionosphere by IR emission from H_3^+ [*Drossart et al.*, 1993; *Miller et al.*, 1997; *Waite et al.*, 1997] both tend to increase τ_H and maintain hydrostatic equilibrium. It is therefore uncertain whether hydrostatic equilibrium is a valid assumption for the auroral atmosphere.

We assume, for the purposes of this paper, that the auroral (and global) atmosphere is in hydrostatic equilibrium. We investigate relatively low (subsonic) horizontal velocities in this study (see Appendix A), which do not invalidate this assumption. We do not include cooling due to IR H_3^+ emission in our model, in order to see what eventual effect this has on the global temperature distribution. We aim to relax these constraints in future model calculations, which will also require careful consideration of the consequences for hydrostatic equilibrium.

Assuming vertical hydrostatic equilibrium, then, the following equality holds :

$$\frac{\partial P}{\partial z} = -\rho g \tag{4}$$

(where ρ is mass density and g is local magnitude of gravitational acceleration). Using equation (4), it can be shown that the horizontal gradients (∇_z and ∇_P) of any scalar, a, in the local Cartesian and P coordinate systems are related as follows [*Fuller-Rowell and Rees*, 1980] :

$$\nabla_z a = \nabla_P a + \rho \nabla_P \Phi \frac{\partial a}{\partial P} \tag{5}$$

where $\Phi = gz$ is the gravitational potential. For the special case of $a = P$, equation (5) yields the result

$$\nabla_z P = \rho \nabla_P \Phi \tag{6}$$

If we combine equations (6), (3) and (2), we arrive at the form of momentum equation used in our numerical model :

$$\left(\frac{\partial \boldsymbol{v}}{\partial t}\right)_P = -\boldsymbol{v} \cdot \nabla_P \boldsymbol{v} - w\frac{\partial \boldsymbol{v}}{\partial P} - \nabla_P \Phi + \boldsymbol{F} \tag{7}$$

Since the pressure levels are logarithmically spaced, derivatives with respect to pressure are conveniently computed in terms of derivatives with respect to n, the integer labeling pressure level. Equation (1) indicates the following equivalence :

$$\frac{\partial}{\partial P} \equiv \frac{-1}{\gamma P}\frac{\partial}{\partial n} \tag{8}$$

For completeness, we now list the separate components of the acceleration $\boldsymbol{F}$, due to Coriolis force, viscosity, and ion/neutral collisions. These are identical in form to those used by *Fuller-Rowell* [1981] and *Fuller-Rowell and Rees* [1980]. Where appropriate, we give these terms in both local Cartesian and P coordinate representations. These transformations have been calculated with the aid of the scalar gradient transform in equation (5), and the equation of hydrostatic equilibrium (4), which indicates the equivalence of the operators $\frac{\partial}{\partial z}$ and $-\rho g \frac{\partial}{\partial P}$. We have also made use of the following transformation equation for the 2-D (horizontal) divergence of a general vector $\boldsymbol{A}$ with only x and y components (which follows from equation (5)):

$$\nabla_z \cdot \boldsymbol{A} = \nabla_P \cdot \boldsymbol{A} + \rho \nabla_P \Phi \cdot \frac{\partial \boldsymbol{A}}{\partial P} \tag{9}$$

The extra acceleration terms in $\boldsymbol{F}$ are Coriolis acceleration, viscosity, and ion/neutral collisions.

2.1.1. Coriolis acceleration. The Coriolis "pseudoforce" which arises in our rotating frame of reference generates an acceleration which is approximated by

$$\boldsymbol{F_c} \approx -2(\boldsymbol{\Omega} \times (v_x, v_y, 0))_{2d} \tag{10}$$

where the subscript $2d$ indicates taking the horizontal component of its associated vector. The vector $\boldsymbol{\Omega}$ represents the angular velocity of the model planet. It may be written in Cartesian/P coordinates as $\boldsymbol{\Omega} = (2\pi/T_{rot} - v_y/2R_J \sin\theta)(-\sin\theta, 0, \cos\theta)$, where θ is rotational colatitude, T_{rot} is the rotational period of the planet ($T_{rot} = 9.925$ hours for Jupiter), and R_J is its radius ($R_J = 7.1398 \times 10^7$ m).

2.1.2. Viscosity. The viscous force in our horizontal momentum equation arises from the vertical transport of horizontal momentum via intermolecular collisions. The j component (j may be x or y) of the corresponding acceleration imparted to the neutral gas is

$$\begin{aligned}(\boldsymbol{F_v})_j &\approx \frac{1}{\rho}(\mu_m + \mu_t)\nabla^2 v_j \\ &+ \frac{1}{\rho}\frac{\partial}{\partial z}((\mu_m + \mu_t)\frac{\partial v_j}{\partial z}) \\ &\approx \frac{(\mu_m + \mu_t)}{\rho}\nabla_P^2 v_j \\ &+ g^2\frac{\partial}{\partial P}((\mu_m + \mu_t)\rho\frac{\partial v_j}{\partial P})\end{aligned} \tag{11}$$

Here, μ_m and μ_t are the coefficients of molecular and turbulent viscosity, which were calculated as a function of temperature T as follows :

$$\begin{aligned}\mu_m &= ([\mathrm{H}]/N)\mu_{\mathrm{H}} + ([\mathrm{H_2}]/N)\mu_{\mathrm{H_2}} \\ &+ ([\mathrm{He}]/N)\mu_{\mathrm{He}} \\ &= ([\mathrm{H}]/N)\mu_{\mathrm{o,H}}T^{\beta_{\mathrm{H}}} + ([\mathrm{H_2}]/N)\mu_{\mathrm{o,H_2}}T^{\beta_{\mathrm{H_2}}} \\ &+ ([\mathrm{He}]/N)\mu_{\mathrm{o,He}}T^{\beta_{\mathrm{He}}}\end{aligned} \tag{12}$$

where N is the total number density of particles and the μ_o and β terms in Table 1 give coefficients in agreement with viscosity measurements [*Lide*, 1997], to within 5%, over the temperature range of the model.

The turbulent viscosity coefficient is given by [*Fuller-Rowell*, 1984]:

$$\mu_t = 2\kappa_t / c_P \tag{13}$$

where κ_t is the coefficient of turbulent thermal conduction and c_P is the heat capacity per unit mass of thermospheric neutral gas (section 2.2). Using $\kappa_t = c_P \rho K$ (see equation (25)), μ_t may also be expressed as $2\rho K$, where ρ is density and K is the eddy diffusion coefficient (section 2.4). At the homopause, $\rho \sim 3 \times 10^{-10}$ g cm^{-3}, $K \sim 1.4 \times 10^6$ cm^2 s^{-1} and $\mu_t \sim 8 \times 10^{-4}$ g cm^{-1} s^{-1}. At the upper boundary of our model, μ_t is typically a factor of 1000 higher than its value at the homopause.

2.1.3. Ion/neutral collisions. The motion of ions and electrons constitutes a current which exerts an electromagnetic (EM) body force on the neutral thermospheric gas through which it flows. The corresponding acceleration is

$$\boldsymbol{F_L} = \boldsymbol{J} \times \boldsymbol{B} / \rho \tag{14}$$

where $\boldsymbol{J}$ represents current density and $\boldsymbol{B}$ is the local magnetic field. This is the most uncertain term in the momentum equation, since it requires knowledge of the planetary magnetic and electric fields. For the simulations described in this study, we assumed a global magnetic field structure given by the offset tilted dipole (OTD) model [*Acuña et al.*, 1983]. Calculation of the current density $\boldsymbol{J}$ requires, in addition, an accurate knowledge of the conductivities in the Jovian ionosphere and the electric fields which prevail there.

To calculate realistic electrical conductivities, we computed the mobilities of electrons and ions using collision rates obtained from the results of *Danby et al.* [1996] (for electron/H_2 scattering) and *Geiss and Bürgi* [1986] (for electron/II and ion/II scattering). We assumed identical cross sections for a particular ion scattering from H and H_2. We ignored scattering from He, since it stays at a relatively small concentration throughout our model thermosphere ($\lesssim$10% of total number density).

Table 1. Parameters Used in Viscosity Calculations

Parameter	Value
$\mu_{o,H}$	2.0715×10^{-7}
μ_{o,H_2}	1.4648×10^{-7}
$\mu_{o,He}$	4.3338×10^{-7}
β_H	0.716
β_{H_2}	0.716
β_{He}	0.670

Units of $\mu_o T^\beta$ (where T is temperature) are kg m^{-1} s^{-1}.

For the electric field of the model, we assumed a modified version of Earth's electric field structure, upon which we superposed a component due to the breakdown in plasma corotation which occurs beyond ~20 R_J in Jupiter's equatorial plane. Further details are given in Appendix A.

2.1.3.1. Vertical velocity: The vertical velocity v_z in our model is computed from the definition

$$v_z = \frac{Dz}{Dt} = \left(\frac{\partial z}{\partial t}\right)_P + \boldsymbol{v} \cdot \nabla_P z + w \frac{\partial z}{\partial P} \tag{15}$$

where the first term on the right-hand side is the time derivative of altitude z for a point on a constant pressure surface; the second term is the scalar product of the horizontal velocity $\boldsymbol{v}$ and the horizontal gradient of altitude z (evaluated at constant pressure); and the third term involves $w = DP/Dt$, the convective derivative of pressure, which is determined from the equation of continuity (section 2.6).

The final term in equation (15) may be rewritten as

$$w \frac{\partial z}{\partial P} = \frac{-w}{\rho g} \tag{16}$$

using the condition of hydrostatic equilibrium (equation (4)).

2.1.3.2. Boundary Conditions: The boundary conditions imposed on the model velocity field are as follows.

1. At the lower boundary, $v_x = v_y = 0$ and constant altitude $z = 357$ km ($P = P_1 = 2$ μbar pressure level), with altitude zero at $P = 1$ bar, situated a distance R_J from the planet center.

2. The v_x (v_y) at the upper boundary equals v_x (v_y) at the adjacent pressure level for the same latitude and longitude

3. At the upper boundary, $w = DP/Dt = 0$ and is determined from the continuity equation (section 2.6) at other pressure levels.

The first boundary condition is arbitrary and will have to be relaxed in future calculations which attempt to connect the model thermosphere to a realistic distribution of stratospheric velocity. The second boundary condition physically corresponds to the breakdown of the fluid-like properties of the neutral gas with increasing altitude, and the corresponding decrease in hydrodynamic momentum transfer.

2.2. Energy Transport

The appropriate equation for energy transport is derived from the basic equation describing the change in enthalpy (per unit mass of thermospheric neutral gas) :

$$c_P \frac{DT}{Dt} - \frac{1}{\rho} \frac{DP}{Dt} = \dot{Q} \tag{17}$$

Here c_P is the heat capacity (at constant pressure) per unit mass of the gas. Since the gas is composed of three

components (H, H_2 and He), c_P needs to be computed using the contributions from each component gas. For temperatures $\lesssim$2000 K, appropriate for Jupiter, c_P may be expressed as

$$\begin{aligned} c_P &= \sum_{j=1}^{3} n_j m_j c_{Pj} / \sum_{j=1}^{3} n_j m_j \\ &= \sum_{j=1}^{3} n_j m_j (M_j/2+1)(k/m_j) / \sum_{j=1}^{3} n_j m_j \end{aligned} \quad (18)$$

where M_j is the number of degrees of freedom per molecule (with mass m_j) of the jth species ($M = 3$ for monatomic H and He, and $M = 5$ for diatomic H_2). As before, n_j denotes number density of the jth species. The heat capacities computed using (18) are in agreement with experimental results obtained over the temperature range of the model [*Lide*, 1997].

The term $\dot{Q}$ in equation (17) represents local heating and cooling processes, such as particle precipitation, solar heating, Joule heating, and thermal conduction. We shall consider each of these processes in this section. The extremely efficient cooling of the auroral ionosphere by IR emission from H_3^+ [*Drossart et al.*, 1993; *Miller et al.*, 1997; *Waite et al.*, 1997] is not included in our model at this stage, in order to see what effect this has on the eventual global temperature distribution. Before we consider the included heating and cooling terms, we now outline the transformation of the basic equation (17) to the P coordinate system.

If we transform the first time derivative in equation (17) into derivatives of coordinates in the P system (as was done for the horizontal velocity in equation (3)), we obtain

$$\left(\frac{\partial h}{\partial t}\right)_P \approx -\boldsymbol{v}\cdot\nabla_P h - w\frac{\partial h}{\partial P} + w/\rho + \dot{Q} \quad (19)$$

where $h = c_P T$ is the enthalpy per unit mass and $w = DP/Dt$, as before. We may also obtain an equation involving the specific horizontal kinetic energy ($e_k = \frac{1}{2}\boldsymbol{v}\cdot\boldsymbol{v}$) from equation (7) by taking the scalar product of both sides with $\boldsymbol{v}$. The result is

$$\left(\frac{\partial e_k}{\partial t}\right)_P = -\boldsymbol{v}\cdot\nabla_P e_k - w\frac{\partial e_k}{\partial P} - \boldsymbol{v}\cdot\nabla_P\Phi + \boldsymbol{v}\cdot\boldsymbol{F} \quad (20)$$

If we now add equations (19) and (20), using equation (4) to eliminate the density ρ, we arrive at the final form of energy transport equation used in our model :

$$\begin{aligned} \left(\frac{\partial(h+e_k)}{\partial t}\right)_P &= -\boldsymbol{v}\cdot\nabla_P(h+e_k+\Phi) \\ &- w\frac{\partial(h+e_k+\Phi)}{\partial P} \\ &+ \boldsymbol{v}\cdot\boldsymbol{F} + \dot{Q} \end{aligned} \quad (21)$$

where $\Phi = gz$ is the gravitational potential. The first two terms on the right side of equation (21) represent the transport of internal energy ($h + e_k$, the total specific enthalpy plus kinetic energy) through bulk motions of the thermospheric gas. These terms also represent, implicitly, the change in internal energy due to the expansion/contraction of a unit mass parcel of moving gas which maintains pressure equilibrium with its surroundings. The third term on the right side of equation (21) represents the power exerted per unit mass of gas by the total of the dynamic forces which it experiences.

We now consider the local heating rate per unit mass $\dot{Q}$ from equation (21). The contribution of particle precipitation to $\dot{Q}$ is considered in section 2.3. We now consider the other contributing heating/cooling terms.

2.2.1. Joule heating. The total Joule heating per unit mass of neutral gas consists of two main contributions: first, the heating due to the dissipation of electrical energy from the current flowing in the medium and, second, the power expended by the EM body ("$\boldsymbol{J} \times \boldsymbol{B}$") force in moving the gas. The total of these rates is

$$\dot{Q}_J = \boldsymbol{J}\cdot\boldsymbol{E}/\rho \quad (22)$$

where $\boldsymbol{J}$ is the local current density and $\boldsymbol{E}$ is the electric field measured in the corotating reference frame of the model.

2.2.2. Solar Heating. The passage of solar EUV photons through the dayside atmosphere of Jupiter deposits an energy flux of $\gtrsim 3.5 \times 10^{-2}$ ergs cm^{-2} s^{-1}, of which approximately 50% goes into heating of the neutral gas [*Waite et al.*, 1983]. To obtain the incident solar flux as a function of wavelength $F_o(\lambda)$, we used the observational data of *Heroux and Hinteregger* [1978], appropriate for solar minimum, and divided by a factor of 27, to account for the dilution of flux in passing from Earth's position to that of Jupiter.

The neutral volume heating rate due to solar EUV radiation at pressure level n of any grid point in our model may be written

$$\dot{Q}_S = f_s \int_\lambda F_u(\lambda)\exp\{-\tau(\lambda,\chi)\}\,d\lambda \quad (23)$$

where $F_u(\lambda)$ is the solar flux per unit wavelength interval, centered on wavelength λ, incident at the upper boundary of the model thermosphere, and f_s is the neutral heating efficiency which we take to be 50%, consistent with the column heating calculations of *Waite et al.* [1983]. The optical depth parameter τ in this case is defined as follows :

$$\tau(\lambda,\chi) = \sum_k \int_{z_o}^{z_u} n_k(z)\;\sigma_k(\lambda)\;\sec\chi(z)\;dz \quad (24)$$

where χ is the local solar zenith angle, z is the altitude which runs from z_o at the depth of interest to z_u at the upper boundary, and the index k denotes a summation over various extinction processes, involving neutral

species of local number density $n_k(z)$ presenting a cross section $\sigma_k(\lambda)$ for photons of wavelength λ. The extinction of solar flux in our model arises from photoionization of H, H_2 and He, as well as photodissociation of the former. References for cross sections can be found in Table 3.

2.2.3. Thermal Conduction. Jupiter's thermosphere shows temperatures which increase monotonically with altitude [*Atreya et al.*, 1981]. This is a defining thermal signature for this atmospheric region, and indicates that thermal conduction is an important means of transporting downwards the energy deposited in the upper thermosphere.

The equation used in our model for the heating rate per unit mass due to thermal conduction (described using molecular and turbulent conduction coefficients κ_m and κ_t) is

$$\begin{aligned}\dot{Q}_m &= \frac{1}{\rho}\nabla_z \cdot \{(\kappa_m + \kappa_t)\ \nabla_z T\} \\ &+ \frac{1}{\rho}\frac{\partial}{\partial z}\left\{(\kappa_m + \kappa_t)\frac{\partial T}{\partial z}\right\} + \frac{1}{\rho}\frac{\partial(\kappa_t \Gamma)}{\partial z} \\ &\approx \frac{1}{\rho}\nabla_P \cdot \{(\kappa_m + \kappa_t)\ \nabla_P T\} \\ &+ g\frac{\partial}{\partial P}\left\{(\kappa_t + \kappa_m)\frac{P}{H}\frac{\partial T}{\partial P} - \kappa_t \Gamma\right\} \end{aligned} \quad (25)$$

where symbols have their usual meaning, $\Gamma = g/c_P$ and $\kappa_t = c_P \rho K$, where K is the local eddy diffusion coefficient (section 2.4). The first and second terms in equation (25) represent horizontal and vertical heat conduction, respectively.

The molecular conduction coefficient κ_m was calculated as a function of temperature as follows :

$$\begin{aligned}\kappa_m &= ([\mathrm{H}]/N)\kappa_{\mathrm{H}} + ([\mathrm{H_2}]/N)\kappa_{\mathrm{H_2}} \\ &+ ([\mathrm{He}]/N)\kappa_{\mathrm{He}} \\ &= ([\mathrm{H}]/N)\kappa_{\mathrm{o,H}} T^{\gamma_{\mathrm{H}}} + ([\mathrm{H_2}]/N)\kappa_{\mathrm{o,H_2}} T^{\gamma_{\mathrm{H_2}}} \\ &+ ([\mathrm{He}]/N)\kappa_{\mathrm{o,He}} T^{\gamma_{\mathrm{He}}} \end{aligned} \quad (26)$$

Where N is the total number density of particles, and the κ_o and γ terms in Table 2 have been chosen to fit the conductivity measurements [*Lide*, 1997], to within 5% over the temperature range in the model.

The boundary conditions are (1) we assume the temperature T at the upper boundary of the model is equal to the temperature at the next lowest pressure level, at the same latitude and longitude, and (2) we assume a constant temperature of 404 K at the lower boundary (see also section 3).

2.3. Energy Deposition

The neutral species in Jupiter's thermosphere are directly ionized by solar EUV photons on the planet's dayside. They are also ionized by energetic photoelectrons released in such photoionizations and by precipitating energetic particles in the planet's aurorae. A range of 1-D models has been developed to describe the ionization and heating of an atmosphere subject to the passage of photoelectrons and/or precipitating particles. These range from the approximate analytical description of ionization by photoelectron impact used by *Majeed and McConnell* [1991] to the sophisticated numerical treatment of electron transport by *Porter et al.* [1987].

Table 2. Parameters Used in Thermal Conductivity Calculations

Parameter	Value
$\kappa_{o,H}$	2.585×10^{-3}
κ_{o,H_2}	1.262×10^{-3}
$\kappa_{o,He}$	3.7366×10^{-3}
γ_H	0.716
γ_{H_2}	0.876
γ_{He}	0.648

Units of $\kappa_o T^\gamma$ (where T is temperature) are J s^{-1} m^{-1} K^{-1}.

We used a simplified "downstream" model to describe the ionization and deposition of energy in the JIM thermosphere by photoelectrons and auroral electrons, based on the expressions of *Nagy and Banks* [1970]. Our expression for the flux $\Phi(E)$ of electrons per unit energy interval, centered on energy E, at altitude z, is

$$\begin{aligned}\Phi(E) &= \Phi_o(E_o)\,(dE_o/dE) \times \\ &\exp\{-\int_z^{z_u} \sigma_R(E')\,dz'/\sin|i|\cos\theta_p\} \\ &+ \int_z^{z_u} q(E')(dE'/dE) \times \\ &\exp\{-\int_z^{z'} \sigma_R(E'')\,dz''/\sin|i|\cos\theta_p\}\,dz' \end{aligned} \quad (27)$$

where $\Phi_o(E_o)$ is the flux of auroral electrons per unit energy interval, with initial energy E_o, incident at the top of the thermosphere. We use $E_o = 10$ keV and choose a non-zero $\Phi_o(E_o)$ at each point within our model auroral ovals, such that the incident energy flux has a component of 8 ergs cm^2 s^{-1} parallel to the local magnetic field. These auroral ovals consist of all surface points with magnetic l parameters between $l_1 = 7$ and $l_2 = 15$ (see Figure 1 and Appendix A for definition of l), chosen to correspond to the 6 R_J and 30 R_J L shells of the O6-plus-current-sheet field model [*Connerney*, 1993]. In order to perform a future investigation of the effects of more realistic, narrower auroral zones, we will need to increase the spatial resolution of our model.

In equation (27), $q(E')$ is the volume production rate per unit energy interval of photoelectrons with energy

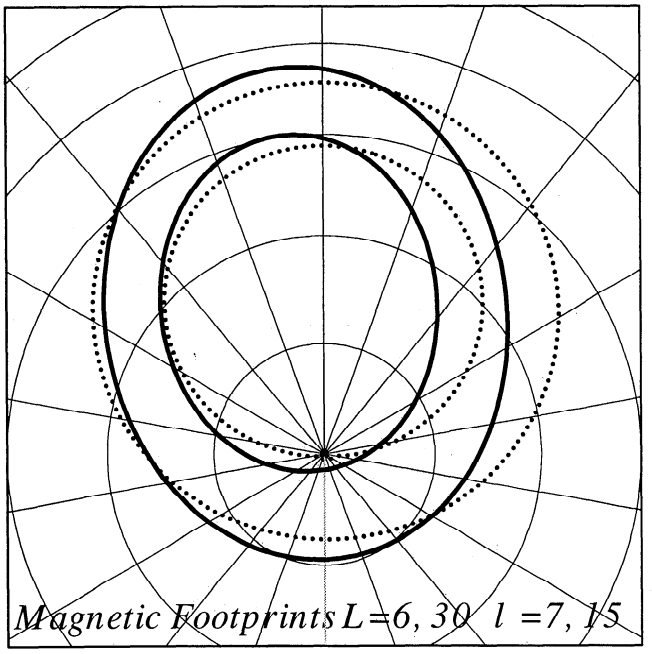

Figure 1. Comparison between the northern $l = 7$ and $l = 15$ footprints of the OTD field model (dotted curves) and the $L = 6$ R_J and $L = 30$ R_J footprints (solid curves) of the O6 field model.

E', i is the local magnetic dip angle, and θ_p is the pitch angle of the energetic electrons with respect to the local magnetic field (we use $\theta_p = 30°$). For completeness, we have included the recombination cross section σ_R, which is also a function of electron energy, but this has negligible effect on the function $\Phi(E)$ for superthermal energies.

The symbol z_u in equation (27) denotes the altitude of the upper boundary of the model thermosphere. In the first term of the equation, representing the contribution from auroral particle precipitation (which is only nonzero inside the auroral ovals), the mean electron energy is E_o at altitude z_u, which decreases to E at altitude z. The energy E' is the mean energy per electron at an intermediate altitude z'. It is important to note that the precipitating electrons in our model have a monochromatic distribution and so $\Phi_o(E_o)$ is nonzero for only one particular value of E_o (10 keV, in this case).

The second term of equation (27) represents the contribution from photoelectron production. A photoelectron of energy E' produced at altitude z' ($z < z' < z_u$) loses energy through inelastic collisions as it spirals about the local magnetic field line and penetrates down to an altitude z, where its energy is E. For any intermediate altitude z'', the energy of this same electron is E''. The equation of energy degradation which allows us to trace the mean electron energy E as a function of altitude z is

$$\frac{dE}{dz} = -\sum_k n_k(z)\ \sigma_k(E)\ \epsilon_k / \sin|i| \cos\theta_p \qquad (28)$$

where the summation is over the variety of ionization and excitation reactions that cause the electrons to lose energy as they propagate. In general, these reactions involve a neutral atom or molecule of number density n_k, which presents an excitation/ionization cross section $\sigma_k(E)$ to an electron of energy E greater than the threshold energy ϵ_k of the reaction. For our model, the specific reactions of excitation/ionization by electrons are listed in Table 3.

The corresponding energy deposited into neutral heating per unit volume, at altitude z, by the propagating photoelectrons is given by

$$\dot{Q}_a = \int_E f_d\ \Phi(E)\ \frac{dE}{dz} \sin|i| \cos\theta_p\ dE \qquad (29)$$

In this expression, f_d is an efficiency factor, which we take to be 30% for heating by auroral precipitation (consistent with the results of *Waite et al.* [1983]). The energy deposition by photoelectrons is implicitly included in the calculation of solar heating (section 2.2).

For reasons of computational efficiency, our treatment of energy deposition only considers downward moving photoelectrons, whereas the expressions by *Nagy and Banks* [1970] include contributions from photoelectrons propagating from their point of origin to both lower and higher altitudes. We compute photoelectron flux distributions for a grid of solar zenith angle and magnetic dip angle, every 30 time steps, assuming the neutral composition at the subsolar point. We then interpolate upon this grid, at each time step, to obtain the photoelectron flux at each spatial point in the model. This procedure effects a large reduction in computational time compared to the case where new photoelectron flux profiles are computed at every spatial point.

For similar reasons, we neglect the contribution of secondary electrons and electron scattering to ionization, energy degradation, and heating. This omission tends to shift the locations of ionization maxima and maximum energy deposition to lower altitudes. However, our model closely reproduces many features of more sophisticated 1-D models, particularly the locations and magnitudes of solar and auroral ionization maxima (section 3).

2.4. Diffusion

The three neutral species in our model thermosphere are H, H_2, and He. The scale height for H_2 in the upper Jovian thermosphere ($P \lesssim 1$ nbar) is approximately $H_o = 150$ km (for $T = 1000$ K), while the diffusive coefficient is $D_o > 10^6$ m^2 s^{-1} [e.g., *Atreya*, 1986]. The typical diffusive time scale for H_2 is therefore $H_o^2/D_o \lesssim 6$ hours, which increases with decreasing altitude. Our model treats diffusion in the way described by *Colegrove et al.* [1966], which we repeat here for convenience.

We use the example of computation of vertical diffusive velocities. Let z denote altitude. Let n_i and w_i denote the number density and diffusive vertical velocity of the ith species (for our models, i runs from 1

through 3). The velocities w_i satisfy the simultaneous equations

$$\frac{1}{N}\sum_{j=1}^{3}\frac{n_j}{D_{ij}}(w_i - w_j) = -\frac{1}{n_i}\frac{\partial n_i}{\partial z} - \frac{1}{H_i} - \frac{1}{T}\frac{\partial T}{\partial z} \quad (30)$$

where T is temperature, $N = \sum_{j=1}^{3} n_i$ is total number density; and $H_i = kT/m_i g$ is the diffusive equilibrium scale height of species i with molecular mass m_i, for a gravitational acceleration g (we use $g = 24.5$ m s^{-2}, appropriate for Jupiter).

The above system of equations (30) does not have a unique solution for the velocities w_i (a constant added to each velocity produces another possible solution). To close the system, we measure the diffusive velocities relative to the center of mass of the local gas, which results in the condition

$$\sum_{j=1}^{3} n_i m_i w_i = 0 \quad (31)$$

The symbol D_{ij} denotes the diffusion coefficient corresponding to the movement of (minor) species i through (major) species j. For our models, we used the coefficients of *Mason and Marrero* [1970], corresponding to hydrogen/helium mixtures. To take turbulent diffusion into account, we add the turbulent diffusive velocities w_i' to the solutions w_i. These are given by

$$w_i' = -K\left(\frac{1}{n_i}\frac{\partial n_i}{\partial z} + \frac{1}{H_a} + \frac{1}{T}\frac{\partial T}{\partial z}\right) \quad (32)$$

where K is the eddy diffusion coefficient, which we set equal to $K_1 = 100$ m^2 s^{-1} (nonauroral region), 500 m^2 s^{-1} (auroral region) at the lowest altitude pressure level ($P = P_1 = 2$ μbar), where the total number density is N_1; and to $K_j = K_1/(N_j/N_1)^{1/2}$ at the jth pressure level, where the total number density is N_j (following *Atreya* [1986]). $H_a = kT/m_a g$ is the equilibrium scale height of a species with a molecular weight equal to the mean molecular weight of the gas, $m_a = \sum_{i=1}^{3} n_i m_i / \sum_{i=1}^{3} n_i$. Once the molecular and turbulent diffusive velocities are computed, they can be used in the continuity equation (section 2.6) to determine their effect on the transport of any particular species.

2.5. Chemistry

There are many chemical reactions affecting the concentrations of both neutral and ionic species in the Jovian thermosphere. Near and below the homopause ($P \sim 1$ μbar), the presence of organic molecules introduces an enormous network of ion/molecule reactions [*Strobel and Atreya,* 1983]. For simplicity, we have mostly omitted reactions involving organic molecules from our chemical rate calculations, and concentrate mainly on modeling the regions above the homopause.

The reactions included in our models are listed in Table 3, along with references for corresponding rates and cross sections. The reactions include photoionization, photodissociation, electron impact ionization/dissociation, and radiative/dissociative ion recombination.

It is important to note the rapidity of the protonation of H_2, reaction (19) in Table 3. It has an associated rate constant $\kappa_p \sim 10^{-9}$ cm^3 s^{-1}. The corresponding destruction timescale for H_2^+ is given by $\tau_p = (\kappa_p[H_2])^{-1}$, which lies in the range 10^{-5}–10 s, given the H_2 densities in our model : $10^8 \leq [H_2] \leq 10^{14}$ cm^{-3} (section 3). Reaction (19) therefore destroys H_2^+ on timescales too small for practical modeling (i.e., compared with the rotation time scale of the planet, ~10 hours). We make the assumption, then, that each reaction producing H_2^+ is immediately followed by the conversion of this H_2^+ to H_3^+ via reaction (19).

We now consider the recombination properties of H_3^+ and H^+, the two principal ions in our model. First, H_3^+ is destroyed (above the homopause ($P < 1$ μbar), away from organic molecules) mostly by recombination with electrons, reaction (20) in Table 3. The measurements of *Leu et al.* [1973] yielded a rate constant $\kappa_r(H_3^+)=2.3\times10^{-7}$ cm^3 s^{-1} at 300 K for this reaction. The branching ratio for the recombination was found by *Mitchell et al.* [1983] to be in the range 1:3–1:2 in favor of 3H production. The H_3^+ dissociative recombination rate has proved highly controversial, but these values are close to the presently accepted rate [*Mitchell,* 1990] and recent determination of the branching ratio [*Datz et al.,* 1995].

The timescale for recombination of H_3^+ is given by $\tau_r(H_3^+)=(\kappa_r[e^-])^{-1}$. The electron number density, $[e^-]$, peaks at values of the order of 10^6 cm^{-3} in the auroral ionosphere and 10^4 cm^{-3} in the nonauroral ionosphere (section 3). The respective minimum values of $\tau_r(H_3^+)$, using these electron densities, are thus of the order of 10 s (auroral) and 10^3 s (nonauroral).

The H^+ ion recombines with electrons much more slowly than H_3^+. Reaction (3) in Table 3 reveals that the rate constant for H^+ recombination by this mechanism is typically of the order of $\kappa_r(H^+)\sim10^{-12}$ cm^3 s^{-1} (using a temperature T =1000 K). The recombination timescales for H^+ will correspondingly be a factor of ~10^5 larger than those for H_3^+ and at least ~10 days in magnitude.

The major sink of H^+ ions in JIM is, in fact, the charge transfer reaction (5) in Table 3, where H^+ is neutralized by capturing an electron from vibrationally excited H_2. Although much work has been done in explicitly modeling the populations in the different vibrational levels of H_2 [*Cravens,* 1987], we follow *Majeed and McConnell*'s [1991] method of using a single rate constant, κ_c =10^{-14} cm^3 s^{-1}, to compute the rate of reaction (5), assumed to be given by the expression $\kappa_c[H_2][H^+]$ ($[H_2]$ is total number density of H_2). Using this expression for the rate, we see that the timescale for neutralization of H^+ is given by τ_c =$(\kappa_c[H_2])^{-1}$ and occupies a range of values from 1 s to 10^6 s, correspond-

Table 3. Chemical Reactions Used in Models

Reaction	Rate Coefficient[a]	Reference for Cross Section
1. $H + e^- \longrightarrow H^+ + 2e^-$		*Olivero et al.* [1973]
2. $H + h\nu \longrightarrow H^+ + e^-$		*Gingerich* [1969]
3. $H^+ + e^- \longrightarrow H + h\nu$	$1.66 \times 10^{-10} T^{-0.64}$	*Storey and Hummer* [1995]
4. $H(n=1) + e^- \longrightarrow H(n=2) + e^-$		*Olivero et al.* [1973]
5. $H^+ + H_2(v \geq 4) \longrightarrow H + H_2^+$	10^{-14} ($T_v = 1740$K)	*Majeed and McConnell* [1991]
6. $H^+ + H_2 + H_2 \longrightarrow H_3^+ + H_2$	3.2×10^{-29}	*Atreya and Donahue* [1976]
7. $H^+ + XH^b \longrightarrow X^+ + H_2$	2.3×10^{-9}	*Atreya and Donahue* [1976]
8. $H^+ + XH \longrightarrow XH^+ + H$	1.5×10^{-9}	*Atreya and Donahue* [1976]
9. $H_2 + e^- \longrightarrow H_2^+ + 2e^-/H + H^+ + 2e^-$		*Tawara et al.* [1990]
10. $H_2 + h\nu \longrightarrow H_2^+ + e^-/H + H^+ + e^-$		*Cook and Metzger* [1964]
11. $H_2 + e^- \longrightarrow H + H + e^-$		*Tawara et al.* [1990]
12. $H_2 + h\nu \longrightarrow H + H$		*Cook and Metzger* [1964]
13. $H_2(X^1\Sigma_g) + e^- \longrightarrow H_2(B^1\Sigma_u) + e^-$		*Shemansky et al.* [1985]
14. $H_2(X^1\Sigma_g) + e^- \longrightarrow H_2(C^1\Pi_u) + e^-$		*Shemansky et al.* [1985]
15. $H_2(X^1\Sigma_g, v=0, J=0) + e^- \longrightarrow H_2(X^1\Sigma_g, v=0, J=2) + e^-$		*Tawara et al.* [1990]
16. $H_2(X^1\Sigma_g, v=0) + e^- \longrightarrow H_2(X^1\Sigma_g, v=1) + e^-$		*Tawara et al.* [1990]
17. $H_2^+ + e^- \longrightarrow H + H$	$\sim 10^{-7}$	*Auerbach et al.* [1977]
18. $H_2^+ + e^- \longrightarrow H + H^+ + e^-$		*Peart and Dolder* [1972]
19. $H_2^+ + H_2 \longrightarrow H_3^+ + H$	2×10^{-9}	*Theard and Huntress* [1974]
20. $H_3^+ + e^- \longrightarrow H_2 + H/H + H + H$ (1 : 2)	$\sim 10^{-7}$	*Leu et al.* [1973], *Mitchell et al.* [1983]
21. $H_3^+ + e^- \longrightarrow H + H + H^+ + e^-$		*Peart and Dolder* [1974]
22. $H_3^+ + XH \longrightarrow XH^+ + H_2$	2.4×10^{-9}	*Atreya and Donahue* [1976]
23. $He + e^- \longrightarrow He^+ + 2e^-$		*Green and Sawada* [1972]
24. $He + h\nu \longrightarrow He^+ + e^-$		*Gingerich* [1964]
25. $He^+ + e^- \longrightarrow He + h\nu$	$1.77 \times 10^{-10} T^{-0.65}$	*Storey and Hummer* [1995]
26. $He^+ + H_2 \longrightarrow H_2^+ + He$	2×10^{-14}	*Atreya and Donahue* [1976]
27. $He^+ + H_2 \longrightarrow H^+ + H + He$	8×10^{-14}	*Atreya and Donahue* [1976]

[a]Rate constants have units of $cm^3\ s^{-1}$ and $cm^6\ s^{-1}$ for two- and three-body reactions, respectively. Blanks indicate use of tabulated or graphical data. Approximate numbers are orders of recombination coefficients calculated by us, from such data, for temperature 500 K.

[b]XH represents a generic organic molecule, principal sink of ions near the homopause. We do not explicitly model the XH population but calculate its effect on other constituents by assuming a constant vertical profile, with chemical properties identical to CH_4, and with number fraction $2 \times 10^{-3} e^{-\Delta z/H_x}$ where Δz is altitude above the lower boundary ($\Delta z = 0$) and $H_x = 10$ km.

ing to the range of H_2 densities between the lower and upper boundaries of the model. These preliminary estimates of ion destruction timescales have important bearing on the investigation of global ionization morphology in section 3.

2.6. Continuity

The continuity equation used in our model is based on that of *Fuller-Rowell and Rees* [1980], which expresses conservation of total mass in the P coordinate system. *Fuller-Rowell and Rees* [1980] have given this equation for a mixture in which no chemical reactions occur. If we include the effects of chemistry explicitly, the slightly modified continuity equation (in P coordinates) reads

$$\nabla_P \cdot \boldsymbol{v} + \frac{\partial w}{\partial P} = \frac{1}{\rho} \Sigma_j m_j (q_j - l_j) \qquad (33)$$

where $w = DP/Dt$ and m_j, q_j, and l_j are the mass and the chemical creation and destruction rates (per unit volume), respectively (section 2.5), of the jth neutral species (JIM's three neutral species are H, H_2 and Hc). Equation (33) is integrated to obtain w at each level in the model thermosphere, assuming $w = 0$ as the upper boundary condition (this means that elements of gas at the uppermost pressure level remain on that level, the altitude of which generally varies).

To monitor the time evolution at a fixed pressure level, latitude, and longitude of a particular ion or neutral species, we use a similar continuity equation :

$$\left(\frac{\partial n_k}{\partial t}\right)_P = -\rho \left(\frac{\partial \Phi}{\partial t}\right)_P \frac{\partial n_k}{\partial P} - \nabla_P \cdot (n_k \boldsymbol{v}_k) - \rho \frac{\partial (n_k \boldsymbol{v}_k)}{\partial P} \cdot \nabla_P \Phi + \rho g \frac{\partial (n_k v_{zk})}{\partial P} + q_k - l_k \qquad (34)$$

where n_k is the number density of a neutral or ion species, $\boldsymbol{v}_k$ is the horizontal velocity of this species, and

v_{zk} is its vertical velocity. These velocities are the sum of two components. First, the velocity component of bulk flow is computed as described in section 2.1. For neutral species the second component of velocity is the diffusive velocity, which arises from collisions between neutral atoms and molecules. This velocity is calculated as described in section 2.4. For a charged species, the additional influence of electric and magnetic fields generates an additional drift velocity, which corresponds to the contribution of that species to the total current density. The calculation of electric current density is outlined in Appendices A and B.

The symbols q_k and l_k in equation (34) denote chemical creation and destruction rates, respectively. Other terms on the right-hand side of the equation represent the change in n_k due to transport by winds and diffusion/drift.

The boundary conditions are (1) ion and neutral populations at the upper boundary of the model are computed assuming diffusive equilibrium and (2) the lower boundary of the model is assumed to have a constant, neutral chemical composition (consistent with organic molecules near the homopause region acting as a major sink of H^+ and H_3^+ ions) (see also section 3).

3. Simulations

Having described the construction and physical inputs of JIM, we now consider the results of a simulation of Jupiter's global thermosphere/ionosphere. The model in question is the result of 38.44 hours (34,600 steps, nearly four Jovian rotations) of simulated time evolution of an initially static, neutral (nonionized) and homogeneous thermosphere (the subsolar point is initially at longitude $\lambda_{III} = 0°$ (System III) and latitude 0°N). The initial vertical profiles of neutral composition, temperature, and pressure as a function of altitude are shown in Figure 2. These profiles were taken from the model atmosphere used to analyze auroral emission in the study by *Rego et al.* [1994]. This model atmosphere was itself adapted from a model provided by J. C. McConnell for that study. We are not yet in a position to evaluate the influence of the choice of a "starting profile" on the ultimate steady/quasi-steady state of the model, since these profiles are modified at each time step by a nonlinear set of equations and also because our model has not yet reached a steady state. As the simulation proceeds, photoionization and particle precipitation build up the concentrations of ions in the model, winds are generated, and heating processes alter the temperature distribution. We now consider the final results of our simulation in more detail.

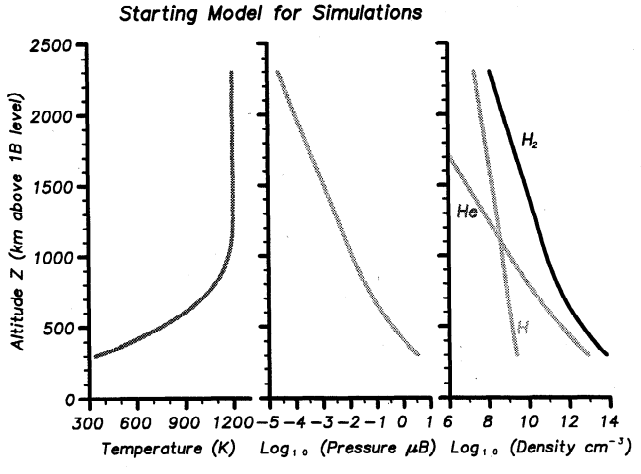

Figure 2. Initial vertical profiles of temperature, pressure, and neutral density as a function of altitude for JIM simulations.

3.1. Global Ionization Morphology

Figure 3 shows contour diagrams of the H^+ and H_3^+ column density over the north polar, south polar, and dayside equatorial regions of the model simulation. The subsolar longitude is at $\lambda_{III} = 304°$. Dark arrows representing horizontal winds (at arrow tail points) on the 1 nbar surface are overplotted on the H^+ distributions. The length of these represents velocity magnitude, as indicated by the scale bars shown.

If we look first at the polar distributions, we see, as we expect, the enhanced levels of H_3^+ and H^+ generated by electron precipitation along the model auroral ovals. The auroral column densities of both ions are slightly higher (by a factor of ~2), in each hemisphere, in the longitude range $200° \lesssim \lambda_{III} \lesssim 100°$. This is due to the magnetic field over this longitude range entering the model planet's surface at a slightly larger angle (i.e., closer to the local normal). Precipitating particles in this longitude range therefore penetrate to deeper layers of the thermosphere, generating higher local ion column densities. H^+ column densities are generally lower than those of H_3^+ in the ionosphere, as a result of our lower assumed column abundance of H compared to H_2 (Figure 2), and the lower overall rate of H^+-producing reactions compared to those producing H_2^+ (and therefore H_3^+).

The localized "spot" of polar ionization on the edge of the auroral oval around $\lambda_{III} \approx 235°$ was formed by an extra precipitation input intended to qualitatively simulate the observed spot-like aurora due to precipitation from the satellite Io [*Connerney et al.*, 1993; *Prangé et al.*, 1996; *Clarke et al.*, 1996]. The size of our model spot spans two resolution elements in longitude and latitude (18° (~5700 km) and 4° (~ 4900 km), respectively). This is larger than the full width at half maximum of the spot's observed UV emission (1000–2000 km [*Clarke et al.*, 1996]). The model's spatial resolution will therefore have to be increased somewhat for future quantitative modeling of this phenomenon.

Precipitation within the spot consists of electrons with the same initial energy (arbitrarily chosen) as those impacting the main auroral oval. The precip-

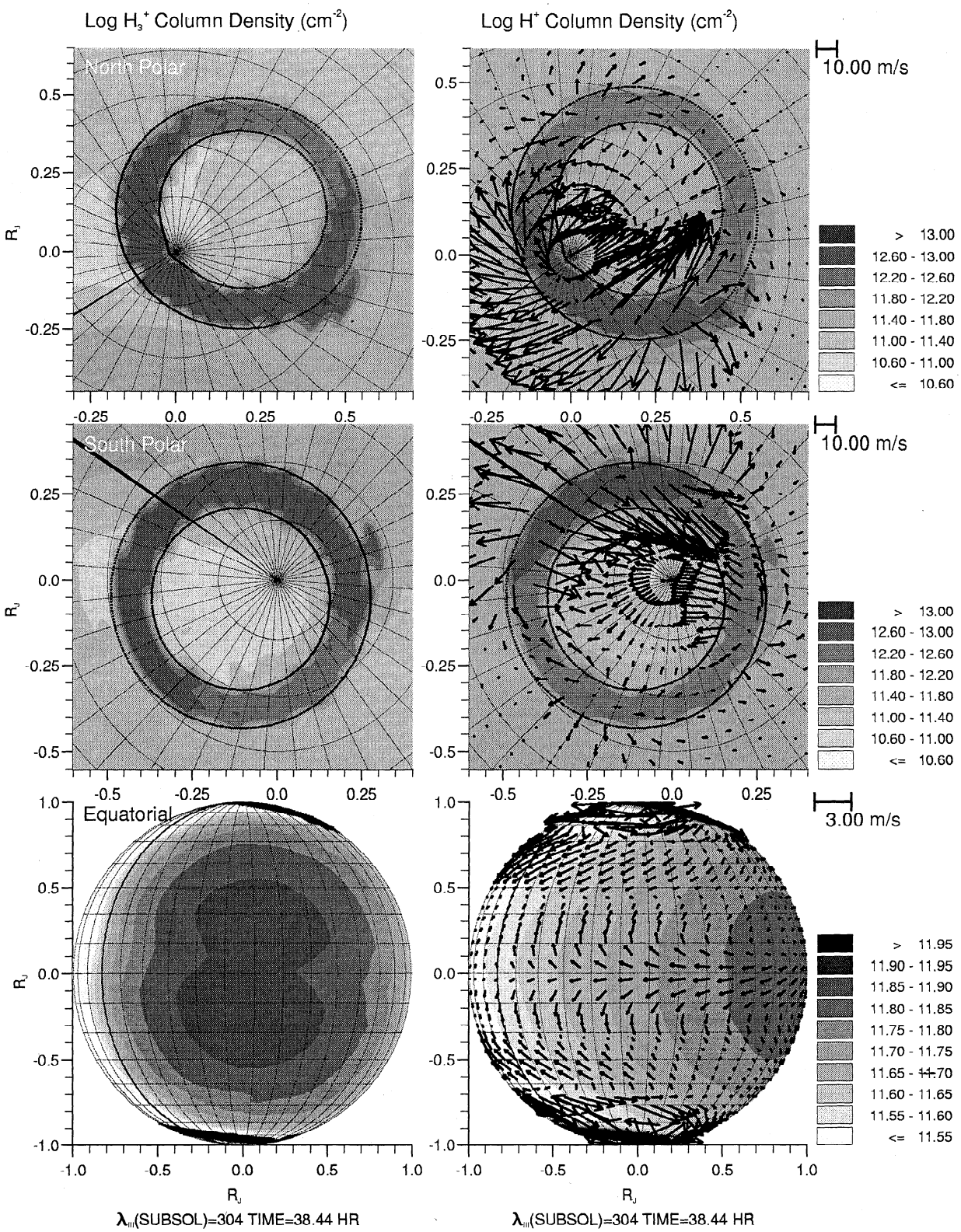

Figure 3. Global ion column densities predicted by JIM. The upper panels show polar column density distributions of H_3^+ and H^+, while the lowest two panels show equatorial distributions (similar to those seen by an Earth-based observer). The H^+ contour diagrams have arrows superposed which represent horizontal wind velocities on the 1 nbar surface, with arrow length indicating speed according to the scale bars shown. The central vertical meridian for all panels is at local noon ($\lambda_{III} = 304°$). Boundaries of auroral precipitation zones are shown as dotted curves. The latitude/longitude grid has a spacing of 10°, and the bold meridian is at $\lambda_{III} = 0°$. Colour figure available at URL http://www.tampa.phys.ucl.ac.uk/nick/cfig.html.

itation flux within the spot is a factor of 3 greater than the main auroral precipitation flux (section 2.3). This corresponds to an energy input of $3 \times 8 = 24$ ergs cm^{-2} s^{-1}, close to the energy dissipation of 30 ergs cm^{-2} s^{-1} deduced by *Clarke et al.* [1996] from their observations. We see that the "trail" of the spot aurora, due to Jupiter rotating with respect to Io, spans $\sim 20°$ in longitude for polar H_3^+ (in the direction of decreasing λ_{III}), but spans $\sim 60°$ for H^+ in the same region. This is due to H^+ being a longer-lived ion than H_3^+ (section 2.5) and therefore remaining longer in the trail of ionized residue generated by the spot aurora until it is neutralized.

The longitudinal span of the H_3^+ and H^+ trails may have important bearing on future comparisons of the observed UV and IR emissions from the Io footprint aurora, since each of these emissions is produced by a different physical mechanism. We predict that recombining H^+ in the relatively long ionization trail will produce a corresponding long trail emission signature in H Lyman α, the component of the UV aurora which is due to radiative deexcitation of H. We also predict that this UV trail will be more extended than the corresponding IR emission from the shorter H_3^+ trail.

The equatorial ionization patterns generally show an increase in column density from the polar regions (large solar zenith angle) toward the equator (small solar zenith angle), as expected from the photoionization process. There is, however, a secondary effect on column density due to magnetic field orientation. This is seen most clearly in the H_3^+ pattern near the equator, where the contour of highest column density has a "pinched" appearance. This pinching occurs along the magnetic equator and is a result of the near-horizontal orientation of the magnetic field in this region, preventing ionizing photoelectrons from penetrating to the deeper layers of the thermosphere. This results in a local minimum in ion column density along the magnetic equator.

The most remarkable feature of the equatorial ionization patterns is the contrast between the local time dependence of the H_3^+ and the H^+ distributions. These are shown in full detail in Figure 4 as "unrolled" cylindrical projections of the surface ionization patterns for the entire model planet. H_3^+ has its maximum column density, in general, near the subsolar point of the planet. The slight asymmetry of the H_3^+ pattern about local noon arises because of the finite time required for the ion to recombine ($\gtrsim 10^3$ s, section 2.5). Consider the following general expression for the number density of a generic positive ion X^+ at a fixed latitude and longitude, as a function of local time t :

$$[X^+]_t = [X^+]_0 + \int_0^t q(t') e^{-(t-t')/\tau_r} \, dt' \qquad (35)$$

In equation (35), $t = 0$ is taken as dawn, $[X^+]_0$ is the ion density at dawn, q is the instantaneous rate of ion production, and τ_r is the local ion recombination time. For H_3^+ specifically, the photoionization rate of H_2, which contributes to its formation and therefore H_3^+ column density, generally increases from dawn until local noon. At later times the formation rate starts decreasing, but there is now a "delay" in the response of the H_3^+ density, since it takes a finite time for residual ions (formed at and just before local noon) to recombine. The ion density at local time t may thus retain a significant contribution from its past values, at times around $t - \tau_r$ and later. When the local density of H_3^+ predicted by equation (35) is integrated over altitude, the asymmetry in the local density distributions remains in that of the column density.

Let us now consider equation (35) with regard to H^+. We see that, since this ion generally has a much longer lifetime against destruction ($\lesssim 10^6$ s) than H_3^+ (in fact, a lifetime which may be comparable to the rotational period of the planet), we would also expect H^+ to have the more pronounced asymmetry between its prenoon and postnoon distributions. Figures 3 and 4 show that this is indeed the case, with column densities of H^+ monotonically increasing from dawn until dusk.

3.2. Altitude Dependence of Global Ionization

We now consider the altitude dependence of the global ionization patterns of H_3^+ and H^+. Figure 5 shows the local number density distributions of these ions for equatorial views (those seen by an Earth-based observer) of the model planet. Three pairs of ionization patterns are shown for three different pressure surfaces.

3.2.1. The 50 nbar pressure level, ~900 km above 1 bar level. If we consider first the lowest altitude pressure surface ($P = 50$ nbar), a typical destruction time for the H_3^+ ions at this level is $\tau_r(H_3^+) \approx 3800$ s (using electron density $[e^-] \approx 2700$ cm^{-3} from the model's subsolar point at this pressure and following the calculations of section 2.5). For H^+ the destruction time at this pressure level's subsolar point is $\tau_c \approx 300$ s (corresponding to charge exchange reaction (5) with $[H_2] \approx 3.2 \times 10^{11}$ cm^{-3}). The large difference in these destruction times translates to very different ionization patterns for each ion at this altitude (equation (35)). The H_3^+ pattern shows marked morning/afternoon asymmetry, since these ions survive, on average, for ~10% of a Jovian day and may thus be carried through ~36° by planetary rotation, starting from their time of formation. The H^+ ions, on the other hand, having much smaller lifetimes, can only be carried a few degrees of rotation before being neutralized. This explains the high degree of symmetry of the H^+ pattern about the subsolar point.

The local minimum in $[H_3^+]$ along the magnetic equator at this pressure level is indicative of photoelectron impact contributing significantly to the formation of this ion, since the depth to which photoelectrons penetrate is sensitive to magnetic field orientation. No such

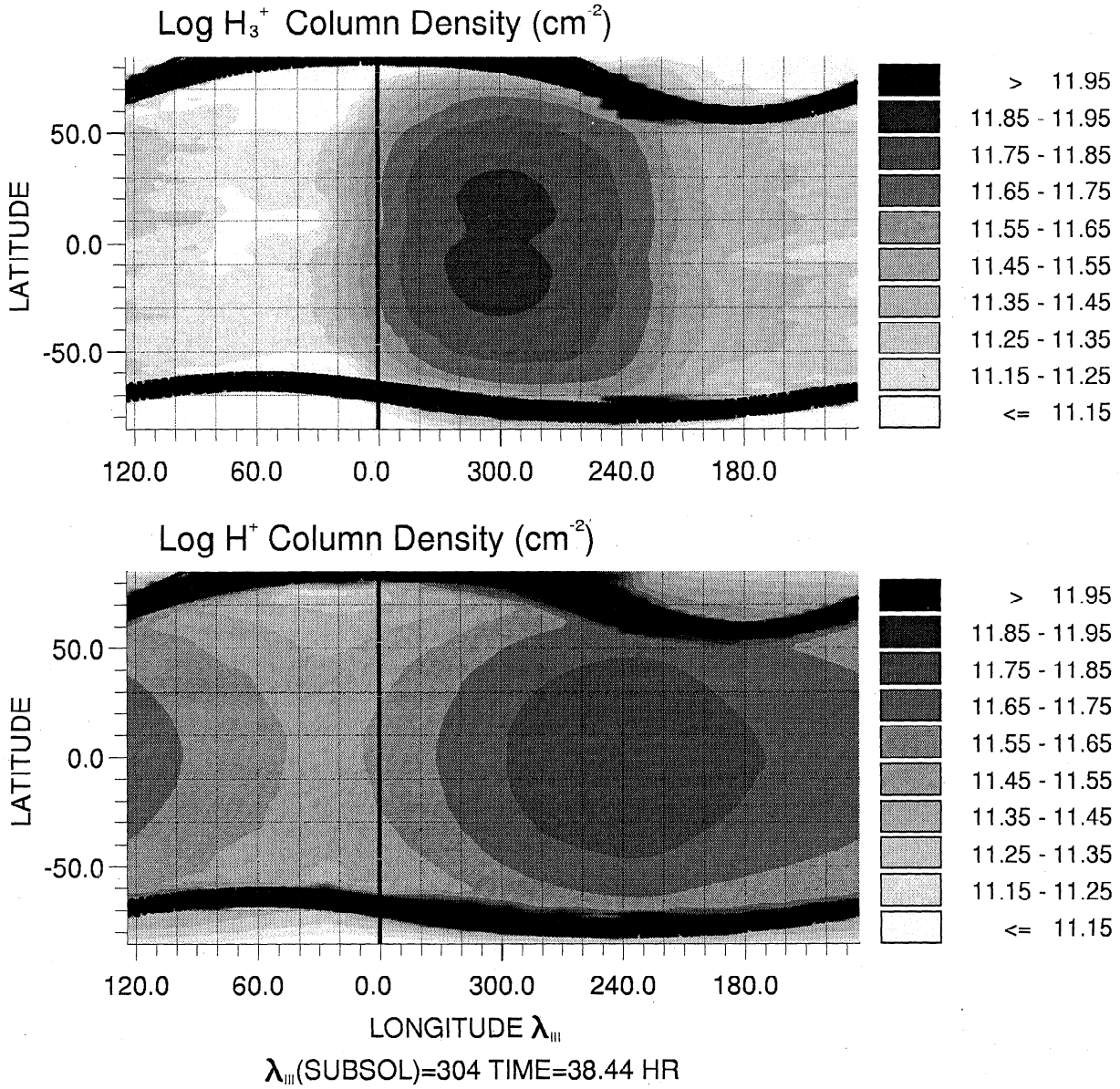

Figure 4. Global ion column densities predicted by JIM – cylindrical projection. The panels show global column density distributions of H_3^+ and H^+ The central vertical meridian for both panels is at local noon ($\lambda_{III} = 304°$). Boundaries of auroral precipitation zones are shown as dotted curves. Colour figure available at URL http://www.tampa.phys.ucl.ac.uk/nick/cfig.html.

minimum is seen in the H^+ pattern. This is because the strongly dominant ionization mechanism for H at this level is still photoionization by solar radiation. Radiation with wavelengths in the interval $845 \leq \lambda \leq 912$ Å can photoionize H but cannot photoionize or photodissociate H_2 (except through Rydberg state predissociation, not included in our cross sections). Photons with these wavelengths have a much higher flux at the homopause than those with smaller wavelengths, which are used up in ionization and dissociation of H_2, the most abundant neutral species.

3.2.2. The 5 nbar pressure level, ~1300 km above 1 bar level. We now consider the 5 nbar pressure surface, located ~400 km above the 50 nbar surface. Here, the destruction time for the H_3^+ ions is $\tau_r(H_3^+) \approx 1200$ s (using electron density $[e^-] \approx 8300$ cm^{-3} from the model's subsolar point at this pressure). The H^+ destruction time at this pressure and at the model subsolar point is $\tau_c \approx 3200$ s (corresponding to $[H_2] \approx 3.2 \times 10^{10}$ cm^{-3}). The destruction times are now of the same order of magnitude, and this is reflected in the similar global ionization patterns. H^+, having the longer destruction time, also exhibits a higher degree of morning/afternoon asymmetry in its distribution. Both ion distributions display the characteristic equatorial pinching in their contour levels associated

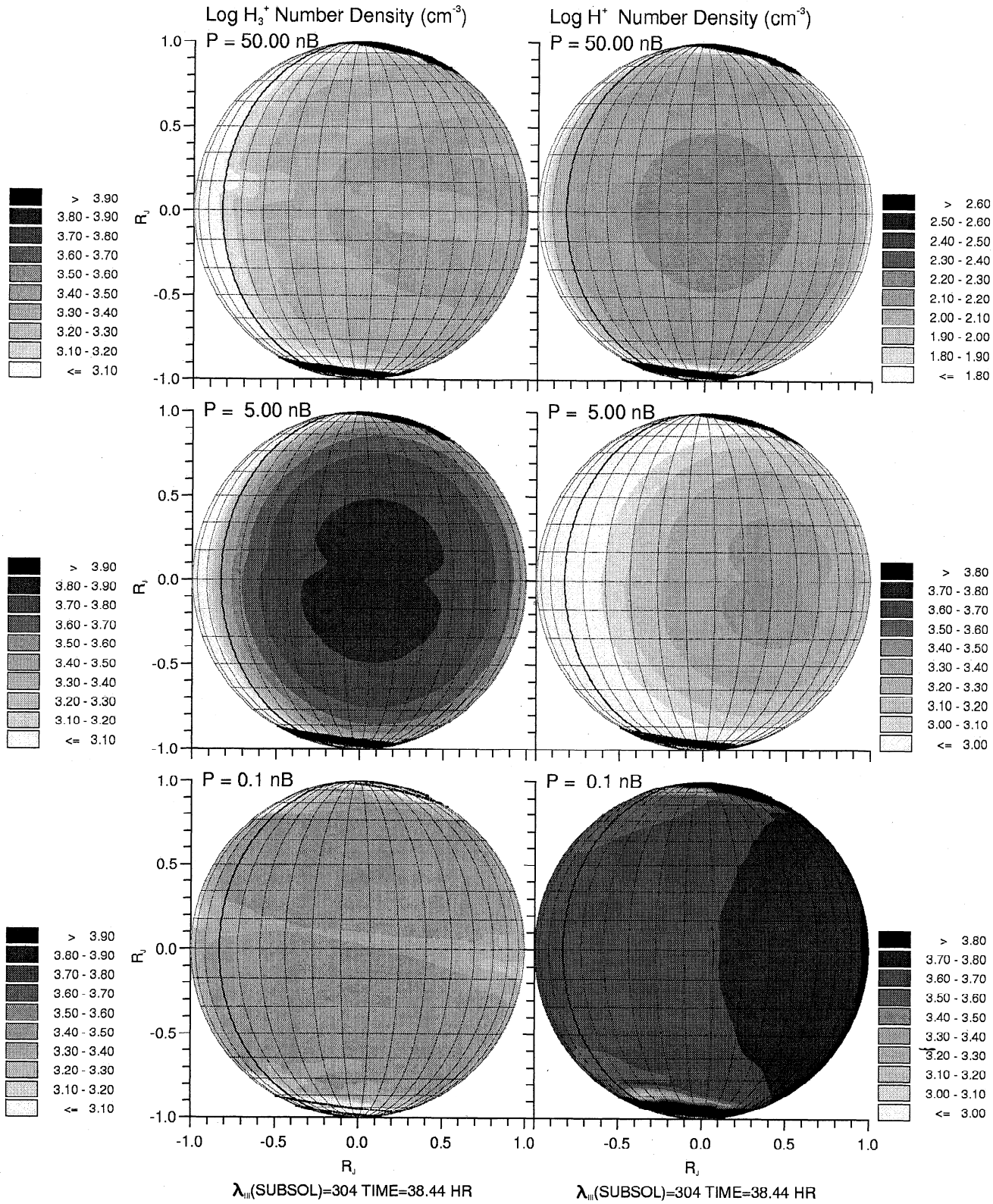

Figure 5. Global local ion densities predicted by JIM, as a function of altitude. All panels show local number density distributions of H_3^+ and H^+ as a function of the indicated pressure level. All distributions are equatorial. The central (noon) meridian for all panels is at local noon ($\lambda_{III} = 304°$). Boundaries of auroral precipitation zones are shown as dotted curves. The latitude/longitude grid has a spacing of 10°, and the bold meridian is at $\lambda_{III} = 0°$. Colour figure available at URL http://www.tampa.phys.ucl.ac.uk/nick/cfig.html.

with the secondary influence of magnetic field orientation on ionization, which we have already discussed (section 3.1).

3.2.3. The 0.1 nbar pressure level, ~2000 km above 1 bar level.. The 0.1 nbar pressure surface is located ~700 km above the 5 nbar surface. At this high altitude the electron density is $[e^-] \approx 7100$ cm^{-3} at the model subsolar point, and this gives a destruction time for H_3^+ ions of $\tau_r(H_3^+) \approx 1700$ s, similar to that at the 5 nbar level. The H^+ destruction time at this pressure, however, is $\tau_c \approx 10^5$ s (>2.5 Jovian days, corresponding to $[H_2] \approx 10^9$ cm^{-3} at the model subsolar point). Once again, the very different destruction times produce strongly contrasting ionization patterns. Being extremely longlived, the H^+ ion density increases monotonically from dawn until dusk.

The H_3^+ pattern shows the local minimum along the magnetic equator, which is seen at all pressure levels for this ion. The influence of reaction (5), followed by reaction (19) (Table 3), as a source of H_3^+ is also apparent at this level. The more uniform distribution of H_3^+ across the globe is due to the higher abundance and more uniform distribution of H^+ here, which makes a significant contribution to the H_3^+ formation rate through this sequence of reactions. We also see in Figure 5 that there is substantially less H_3^+ than H^+ in the auroral regions. This is a natural long-term consequence of the model's chemistry, which we consider in section 3.4, after examining the effects of wind transport on ionization distributions.

3.3. Auroral Ionization and Winds

The fastest winds in Figure 3 on the nbar surface occur in the strong outflow region situated at longitudes $220° \lesssim \lambda_{III} \lesssim 70°$ at the boundaries of the auroral ovals. This outflow, characterized by wind speeds up to 35 m s^{-1}, is predominantly driven by a large pressure gradient between the inside and outside regions of the ovals or, equivalently (for a constant-pressure surface), a large altitude gradient (equation (6)). As described in section 3.4, it is the difference in chemical composition and the consequent effect on altitude that is mainly responsible for these gradients at this pressure level. It is important to note that a more realistic, narrower auroral zone with a higher energy input from particle precipitation would result in higher outflow velocities. We would need to increase the spatial resolution of JIM to accurately model auroral zones significantly narrower than those used in this paper (see section 2.3).

We would also expect temperature gradients to form, since particle precipitation heats the auroral regions. However, the energy of the precipitating electrons is mostly deposited at pressure levels $\gtrsim 0.1$ μbar (section 3.4 [*Kim et al.*, 1992; *Trafton et al.*, 1994]) at altitudes far below the 1 nbar surface. We require a finer vertical resolution at these lower altitudes in order to trace more accurately the maximum deposition of energy there by precipitating particles. We leave this to a future study, which will investigate in greater detail the long-term dynamical response of the thermosphere to auroral heating.

Figures 3 and 4 also show the effect of the auroral outflow on the global distributions of H_3^+ and H^+. If we take 1200 s as a typical recombination time for H_3^+ near the 1 nbar level (confirmed by the vertical profiles presented below), then winds with speeds around 35 m s^{-1} may carry H_3^+ ions at this level for a distance of about 40 km during one recombination lifetime. This is negligible compared to the dimensions of a horizontal grid cell at the outflow region (~2500 km (meridional) × 2000 km (azimuthal)). It follows that the winds (at this pressure level) would not be efficient in transporting H_3^+ through significant distances from the auroral ovals. This argument is illustrated and extended to all pressure levels by the appearance of the auroral H_3^+ column densities, which are tightly confined within the boundaries of the precipitation ovals and spot trail.

H^+, being a generally longer lived ion than H_3^+ (section 2.5), will be carried further from the auroral ovals by the outflowing winds. The relevant signature of the H^+ column density distribution is situated at longitudes $250° \lesssim \lambda_{III} \lesssim 320°$, an excursion of auroral H^+ beyond the boundaries of the ovals and "upstream" of the auroral spot. H^+ located here is not produced by auroral processes but is transported by winds from inside the ovals themselves.

Figure 6 shows model vertical profiles of H_3^+ number density, H^+ number density and horizontal wind velocities for points in the auroral and nonauroral ionosphere. If we first consider equatorial ion densities, we find that our profiles have peaks situated close in altitude to those of *Majeed and McConnell*'s [1991] Model E, the published model which best matches our own model inputs. The magnitudes of our model's ionization peaks, however, are about half an order of magnitude smaller than those of *Majeed and McConnell* [1991], but this is probably due to the smaller recombination rate coefficient used by them for H_3^+ (~2.0×10^{-8} cm^3 s^{-1}) and differences in neutral composition.

Let us now consider the auroral ion density profiles. The auroral H_3^+ profile peaks at a pressure of about 0.16 μbar, in agreement with the location of the H_3^+ auroral peak in the model of *Kim et al.* [1992], who also use 10 keV precipitating electrons. Our maximum H_3^+ density, however, is nearly an order of magnitude larger than that predicted by *Kim et al.* [1992]. Moreover, the auroral H^+ peak in Figure 6, produced by particle precipitation, occurs at a similar altitude to that of the H_3^+ peak of 0.16 μbar. By contrast, the model of *Kim et al.* [1992] produces an H^+ maximum at a pressure around 0.08 μbar, which is about 2 orders of magnitude larger in density than that produced by JIM. These differences are very likely due to the lower total precipitation flux (1 erg cm^{-2} s^{-1}) and higher steady

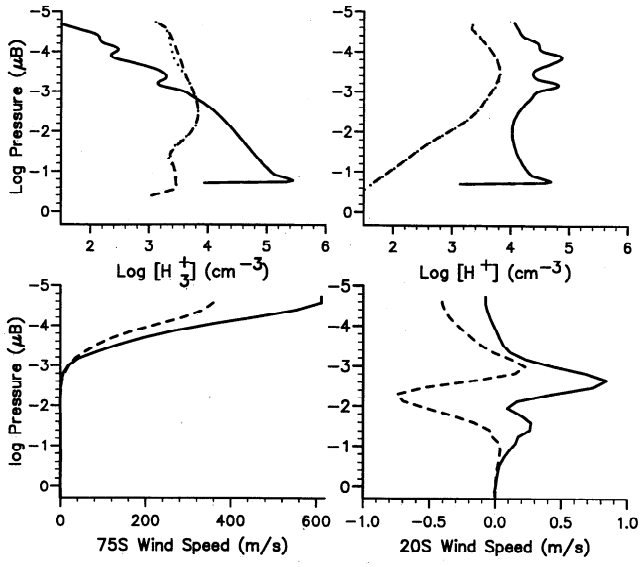

Figure 6. Model vertical profiles of winds and ionization. (upper left) Vertical profiles of H_3^+ number density for points on the subsolar meridian ($\lambda_{III} = 304°$) at latitudes of 4°N (dotted curve) and 20°S (dashed curve); and at latitude 75°S (solid curve), which lies within the southern auroral zone. (upper right) Vertical profiles of H^+ number density for points on the subsolar meridian ($\lambda_{III} = 304°$) at latitudes of 4°N (dotted curve) and 20°S (dashed curve); and at latitude 75°S (solid curve), which lies within the southern auroral zone. (lower left) Vertical profiles of meridional (solid curve) and azimuthal (dashed curve) wind velocity for the point on the subsolar meridian ($\lambda_{III} = 304°$) at a latitude 75°S, which lies within the southern auroral zone. (lower right) Vertical profiles of meridional (solid curve) and azimuthal (dashed curve) wind velocity for the point on the subsolar meridian ($\lambda_{III} = 304°$) at a latitude 20°S.

state H concentrations used by *Kim et al.* [1992] (the latter is caused by particle precipitation; see also section 3.4). The column density of H_3^+ from Kim et al.'s model is a factor of ~6 lower than our peak auroral column density for H_3^+. This is a little lower than the factor of 8 difference between our model's precipitation flux (8 ergs cm^{-2} s^{-1}) and that of *Kim et al.* [1992], which would apply also to the ion column densities, if all other inputs were identical.

The irregular "tongues" of ionization seen at high altitudes in our auroral H^+ density profile result from the transport of this ion by winds. They are superposed on the broad local maximum due to H^+ production by solar radiation. There is no corresponding broad maximum due to photoionization in the H_3^+ auroral density profile. This is due to the depletion of H_2 in the high-altitude thermosphere (section 3.4 [*Kim et al.*, 1992]) and the resulting overall decline in formation of H_2^+ and therefore H_3^+. There are, however, small local minima in the high-altitude H_3^+ density profile which correspond in location to the tongue-like local maxima in the H^+ profile. This is due to the increased local electron density at these altitudes and the subsequent increase in the rate at which H_3^+ recombines.

The high-altitude dependence of horizontal wind velocities in the particular auroral profile of Figure 6 shows a monotonic increase toward the upper boundary of the model, where these velocities are $\lesssim$600 m s^{-1}. The winds in the pressure range $0.03 \lesssim P \lesssim 0.3$ nbar are dominantly driven by a pressure gradient produced by the difference in chemical composition between the auroral and nonauroral thermosphere (section 3.4). The meridional accelerations due to pressure gradients for this pressure/altitude range lie in the interval 0.15–1.10 m s^{-2} (increasing with altitude). The corresponding range in Coriolis acceleration is -0.03 to -0.12 m s^{-2}. We show the various accelerations as a function of altitude in Figure 7. The total acceleration at this stage is nonzero and dominated by pressure gradients. The acceleration due to the EM body force is "self-regulating" and produces changes in velocity which tend to decrease the original "$\boldsymbol{J} \times \boldsymbol{B}$" acceleration. At the simulated time shown, it is the dominant acceleration only at lower altitudes $P \sim 0.1$ μbar. Vertical winds at the same auroral latitude and longitude (75°S,$\lambda_{III} = 304°$) do not exceed ~15 m s^{-1}.

It is important to bear in mind that the minimum timescale, indicated by our simulation, for wind transport over distances comparable to the planet itself is given by $R_J/v \approx 7\times10^7$ m / 600 m s^{-1} $\sim 10^5$ s. This timescale approximately equals 3 Jovian days. We therefore need to run the model through many more planetary rotations before we can begin to probe the

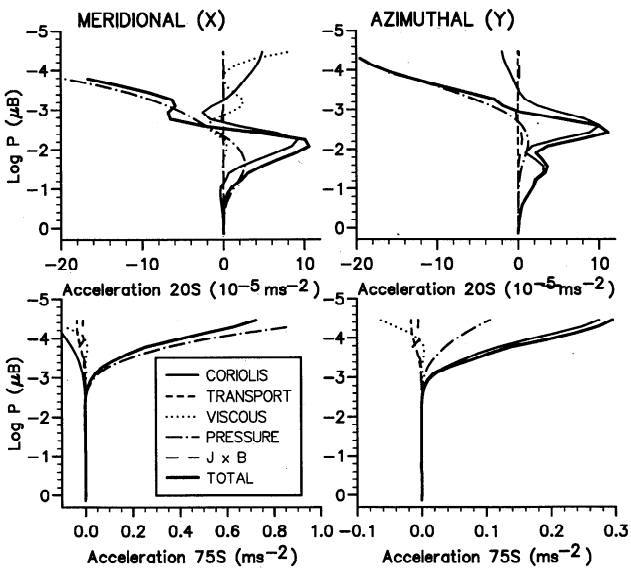

Figure 7. Accelerations in auroral and nonauroral regions. (upper left and right) Meridional and azimuthal accelerations for a point on the subsolar meridian ($\lambda_{III} = 304°$) at latitude 20°S. (lower left and right) Meridional and azimuthal accelerations for a point on the subsolar meridian ($\lambda_{III} = 304°$) at latitude 75°S.

long-term effects of wind transport on the global atmospheric and ionospheric composition and temperature. Since our initial study, JIM has evolved through one additional planetary rotation. By comparing the wind profiles at this later time of 48.44 hours, shown in Figure 8, with those of Figure 6, we see that the wind velocities have not yet reached a periodic steady state. On the other hand, the comparison of the ion profiles in Figures 6 and 8 indicates that most of the global ionosphere appears to attain almost the same density distribution after one rotational period. The main exceptions are the transport-induced tongues in the auroral ionosphere. The remainder of the ion profiles are determined by chemical processes with much smaller timescales.

If we now look at the nonauroral/equatorial wind profile in Figure 6 (latitude 20°S, longitude $\lambda_{III} = 304°$), we find much lower wind speeds $\lesssim 1$ m s^{-1}. The peaks in wind speed occur near the same altitudes as the equatorial ionization peaks and are initially produced by pressure gradients and subsequent Coriolis forces. We show these and other accelerations as a function of altitude in Figure 7. The maximum magnitudes of acceleration due to the dominating pressure gradients and Coriolis forces at this location are $\sim 2.5\times10^{-4}$ m s^{-2} ($P < 10^{-4}$ μbar) and $\sim 10^{-4}$ m s^{-2} ($P = 10^{-2}$–10^{-3} μbar), respectively.

3.4. Neutral Composition and Temperature

Figure 9 shows the temperature and composition of our simulation over a surface of constant longitude. The subsolar (noon) longitude of $\lambda_{III} = 304°$ was used. The temperature deviates significantly from that of the initial model for pressure levels $P \lesssim 10$ nbar. It can be seen that energy has been transported outward from the auroral regions (situated at latitudes 80°N and 75°S in the figure), resulting in a cooling of the high-altitude auroral thermosphere and a local heating of gas situated near the auroral zones. The temperature increase here seems to be propagating in a wave-like pattern. Similar temperature distributions are obtained for longitudes $220° \lesssim \lambda_{III} \lesssim 70°$, corresponding to the extent of the strong outflow region discussed in section 3.3. The temperature distribution is thus a signature of energy being transported out from the auroral regions by these winds.

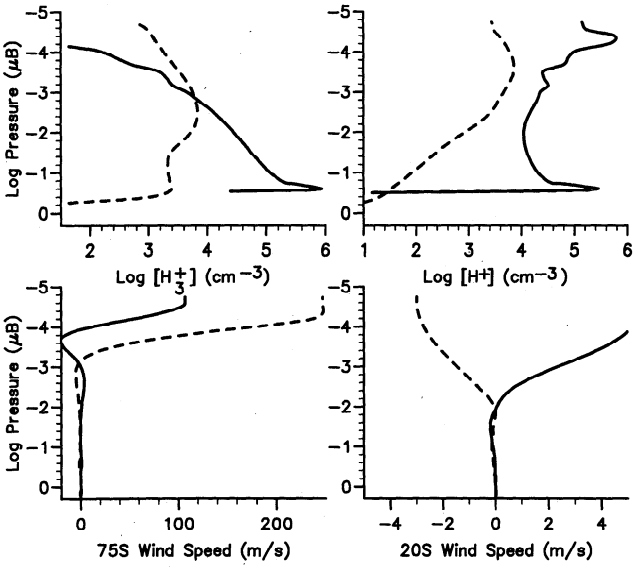

Figure 8. Model vertical profiles of winds and ionization. Panels as for Figure 6 but corresponding to model output at 48.44 simulated hours, or 1 Jovian day after the results of Figure 6.

It must be emphasized that our simulation is not in a steady state and that we require to compute many more rotations before we can assess the long-term effects of energy transport and deposition. For example, the timescale associated with temperature change at the altitude of the auroral ionization peak (0.16 μbar, 580 km above the 1 bar level) is given by $\tau_H = c_P \rho \Delta T / \dot{q}$, where ΔT is the magnitude of the temperature change and $\dot{q}$ is the heating rate per unit volume. To make an estimate of a lower limit for τ_H, let us assume a specific heat $c_P = 1.45\times10^8$ ergs K^{-1} g^{-1} appropriate for H_2, a density $\rho = 3.5\times10^{-12}$ g cm^{-3} (deduced from the pressure and temperature $T = 800$ K at this level, assuming a pure H_2 composition), and a heating rate $\dot{q} = 2.5\times10^{-7}$ ergs cm^{-3} s^{-1} equal to the local precipitation heating rate as shown in Figure 10. For $\Delta T = 50$ K, $\tau_H \gtrsim 17$ hours (2 Jovian days). We therefore need to run the simulation through many more planetary rotations before we achieve long-term stability in the temperature solutions at all altitudes.

Figure 10 shows the major sources of heating as a function of altitude for both auroral and nonauroral locations. The dominant energy sources for the nonauroral thermosphere are solar heating, for pressures $\lesssim 0.01$ μbar, with thermal conduction and transport cooling the thermosphere at lower altitudes. By contrast, the auroral thermosphere shown in the figure is mainly cooled by transport processes (see discussion above) at high altitude and mainly heated by particle precipitation and Joule heating at lower altitudes.

The corresponding distribution of mean molecular mass for the same longitude in Figure 9 shows that the composition of the neutral gas has changed significantly in the auroral regions. The nonauroral thermosphere, on the other hand, shows no significant change in composition compared to the initial profile. The reduction in mean molecular mass in the auroral thermosphere indicates a reduction in the concentration of H_2 and an increase in the concentration of H over the time of the simulation. Similar distributions of composition are seen in the auroral thermosphere at other longitudes.

This change in composition is a natural consequence of the long-term chemistry associated with our model. Reactions (9) through (12) from Table 3, which describe the ionization and dissociation of H_2, all have at least one channel which involves H as a product. Moreover,

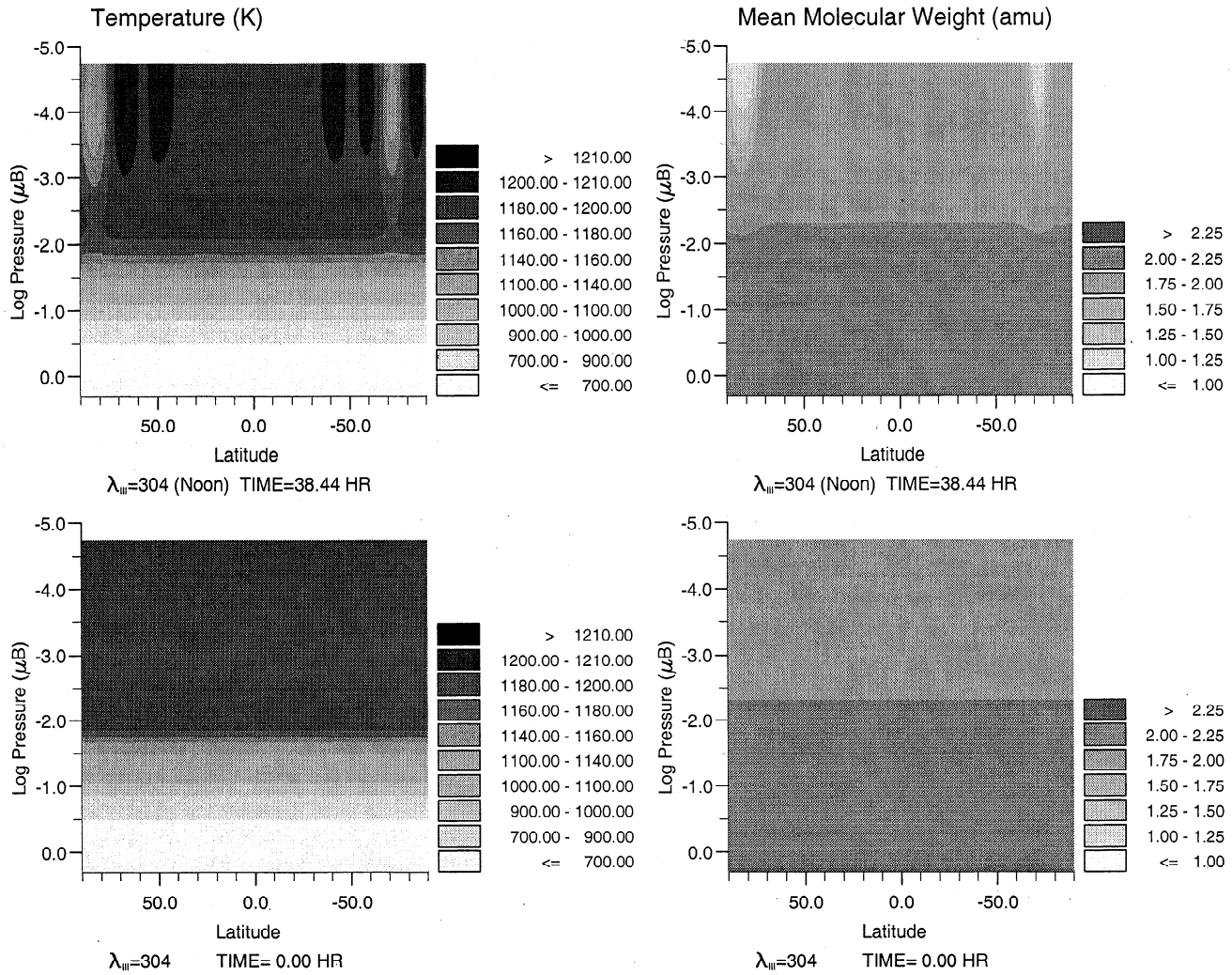

Figure 9. Longitude cuts of temperature and neutral composition. (left) Upper panel shows distribution of temperature over a surface of constant longitude, equal to the subsolar longitude $\lambda_{III} = 304°$. The lower panel shows the initial distribution for comparison. (right) Upper panel shows distribution of mean molecular weight of the neutral gas over a surface of constant longitude, equal to the subsolar longitude $\lambda_{III} = 304°$. The lower panel shows the initial distribution for comparison. Colour figure available at URL http://www.tampa.phys.ucl.ac.uk/nick/cfig.html.

the recombination reactions (20) and (21) always produce at least one H for every recombining H_3^+ ion. Reactions involving organic molecules near and below the homopause, such as (7) and (22), are capable of forming H_2 afresh, however.

Above the homopause therefore we expect chemistry alone to gradually deplete the numbers of H_2 molecules and replace them with H atoms. We would expect this to occur on a shorter timescale in the auroral thermosphere, since H_2 ionization processes there are augmented by particle precipitation. Our simulation results support this notion, with the auroral atmospheric composition being markedly different from that of the rest of the planet. The work of *Waite et al.* [1983] and *Kim et al.* [1992], using 1-D models, also indicates higher steady state H column densities in the auroral, as opposed to the nonauroral, atmosphere. The replacement of molecular hydrogen by atomic hydrogen in our model initially results in higher overall number densities and pressures within the auroral thermosphere. This is what builds up the strong pressure gradients which drive the outflow described in section 3.3.

It is almost certain that dynamic processes also play a part in the replenishment of molecular hydrogen in the auroral thermosphere. New H_2 formed at the homopause could be transported upward by winds (and/or turbulent motion). We may find such winds are generated if we increase the vertical resolution of the low-altitude thermosphere in our model, in order to compute, more accurately, the heating due to the deposition

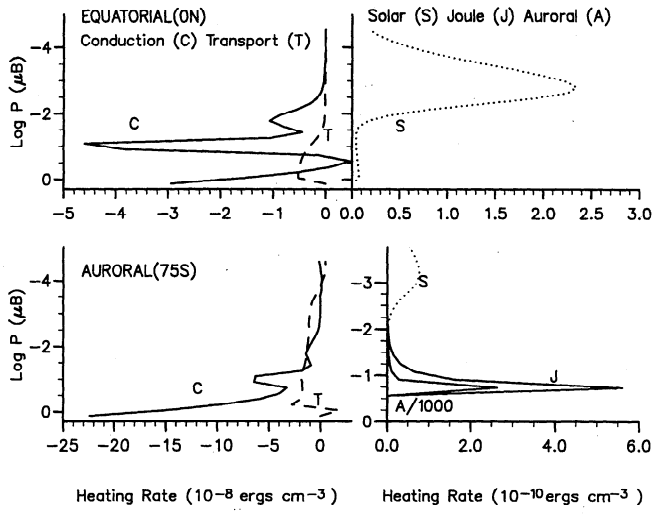

Figure 10. Model vertical profiles of volume heating rates. (upper panels) Vertical profiles of cooling rate due to vertical thermal conduction (C) and wind transport and work terms (T) and of the solar heating rate (S), for a point on the subsolar meridian ($\lambda_{III} = 304°$) at latitude of 0°N. (lower panels) The same profiles, along with heating profiles due to Joule (J) and precipitation (A) heating, for a point on the subsolar meridian ($\lambda_{III} = 304°$) at a latitude 75°S, which lies within the southern auroral zone.

of energy there by precipitating electrons. We intend to use JIM in a future study to further investigate these possibilities.

4. Conclusions

We have described JIM, a time-dependent 3-D model of Jupiter's thermosphere and ionosphere. We have given details of the necessary inputs for computations involving the chemistry, dynamics, and energy transport included in the model.

By considering an illustrative simulation, we have demonstrated the wealth of information that can be gleaned from a model of this nature, including wind speeds, ionization levels, temperature, and neutral composition. More important, the model can also help us understand how these different physical properties influence and interact with each other. Examples of this include the influence of solar photons, magnetic field orientation and particle precipitation on global ionization patterns (section 3.1); the transport of ions, by winds, from auroral to non-auroral regions (section 3.3); the trail-like signature of H_3^+ produced by an Io "footprint"-type aurora and planetary rotation (section 3.1); and the influence of electrodynamic forces and chemical composition on winds (sections 3.3 and 3.4).

Evidently, JIM has strong potential for modeling 2-D images of Jupiter and time-dependent global events on the planet. By revealing relationships between different physical aspects of the planet's atmosphere, modeling studies may also guide the types of observations we need to make, in order to obtain useful diagnostics of some particular property.

Modeling with a spatial grid of higher resolution than that used in this study is desirable in order to model more realistic structures for the auroral zone and higher velocity, probably supersonic, auroral outflows. We also need to run the model for many more planetary rotations in order to probe the long-term effects of (1) wind transport on the atmospheric composition (section 3.3) and (2) energy transport and deposition on the temperature distribution (section 3.4).

We intend to continue our simulation toward a steady-/quasi-steady state, and to track the additional changes in the wind system, temperature, and neutral/ionospheric composition. The physical history thus revealed may help us better understand the presently observed properties of Jupiter's upper atmosphere and their origins.

Appendix A: Electric Field

The magnitude and structure of Jupiter's electric field are unknown. Because we wish to explore flows partly driven by electrodynamical forces, we have employed, for the sake of simplicity, at all pressure levels, the analytical expressions of *Spiro et al.* [1978]. These describe the electric potential induced at Earth's surface by the solar wind impinging on the magnetosphere. We repeat these expressions here for convenience. The electric potential is given by

$$\psi_m = \psi_o(\sin\theta'/\sin\theta'_o)^k(\sin(\phi'-\phi'_\odot)/\sin\phi'_d) \quad (|\phi'-\phi_\odot| < \phi'_d) \quad \text{(A1)}$$

$$\psi_m = \psi_o(\sin\theta'/\sin\theta'_o)^k \mathrm{sgn}(\phi'-\phi'_\odot) \quad (\phi'_d \le |\phi'-\phi_\odot| \le 180°-\phi'_n) \quad \text{(A2)}$$

$$\psi_m = \psi_o(\sin\theta'/\sin\theta'_o)^k(\sin(\phi'-\phi'_\odot)/\sin\phi'_n) \quad (180°-\phi'_n \le |\phi'-\phi_\odot| \le 180°) \quad \text{(A3)}$$

The quantities θ' and ϕ' are magnetic colatitude and longitude, respectively. The reference axis for these coordinates is the axis of symmetry of our adopted magnetic field model, the standard Offset Tilted Dipole (OTD) model (note this axis passes through the location of the dipole, not the center of the planet). Here $\phi'_\odot$ is the magnetic longitude of the Sun in this system. The parameters used to define the structure of the electric potential are as follows: θ'_o is the polar cap boundary (where direction of $\boldsymbol{E} \times \boldsymbol{B}$ -type plasma drift reverses), ϕ'_d is the half-width of the dayside "entry region", ϕ'_n is the half-width of the nightside "exit region", ψ_o is the polar cap potential, and k is the index describing latitudinal variation of electric field.

For the models in this paper, we have used (mostly following *Quegan et al.* [1982] for their terrestrial study) $\phi'_d = 20°$, $\phi'_n = 60°$, $k = 1$ (for polar regions where $\theta' < \theta'_o$ or $\theta' > 180° - \theta'_o$) and $k = -3$ (for $\theta'_o \le \theta' \le 180° - \theta'_o$). We have also arbitrarily set $\theta'_o = 10°$, ap-

propriate for the dimensions of Jupiter's magnetopause; and $\psi_o = 100$ kV (between three and four times the values of Quegan et al.). To the potential ψ_m we add a "breakdown potential" ψ_c. This latter potential is used only on the surface regions of the model planet which lie at the footpoints of magnetic field lines which intersect noncorotating plasma in Jupiter's equatorial plasma disk. The motion of this plasma across magnetic field lines induces an emf in the magnetosphere which projects onto the ionosphere, appearing there as the potential ψ_c. The form of ψ_c we use is

$$\psi_c = \frac{\Delta V}{2}\left\{1+\sin\left[\pi\left(\frac{l-l_1}{l_2-l_1}-\frac{1}{2}\right)\right]\right\} \qquad \text{(A4)}$$

Here we use the l parameter to indicate, for any field line, the distance (in units of planetary radii) at which it intersects the magnetic equatorial plane (which is perpendicular to the magnetic symmetry axis). For our offset dipole field, $l = 1/\sin^2\theta_i'$, where θ_i' is the magnetic colatitude of the surface footpoint of the field line (where the surface is defined as a sphere of radius R_J). We take $l_1 = 7$ and $l_2 = 15$ as the bounding "shells" of field lines inside which the potential ψ_c is applied. We chose $l_2 = 15$ in order to obtain a surface magnetic footprint, for this shell, of approximately the same size as the "30 R_J" ($L = 30$) footprint associated with the more realistic O6-plus-current-sheet field model [*Connerney*, 1993] (see Figure 1).

The quantity ΔV in equation (A4) is the total potential difference between the bounding magnetic shells. A realistic estimate is $\Delta V \approx \delta v_{rot}\ B_{av}\ \Delta L$, where the factors are the mean difference in rotational velocity between the equatorial plasma (which lies between the bounding magnetic shells) and the local rate of corotation, the mean field strength over this same region of plasma, and the equatorial distance between the bounding shells, respectively. If we adopt appropriate values of $\delta v_{rot} \approx 30$ km s^{-1} (assuming 10% lack of corotation for the plasma), $B_{av} = 25$ nT (for a point situated at 25 R_J in Jupiter's equatorial plane) and $\Delta L = 10\ R_J$, we obtain a value $\Delta V \approx 5\times10^5$ V. A potential difference of this magnitude actually produces supersonic velocities, via the resulting "$\boldsymbol{J}\times\boldsymbol{B}$" force [see *Sommeria et al.*, 1995]. We leave the investigation of such flows for a future study and concentrate on subsonic flows alone in this paper. Accordingly, we have used $\Delta V = 10^4$ V in our simulations in order to keep the magnetospheric forcing at a level smaller than expected and to investigate the qualitative effects of this forcing. We have plotted the model magnetospheric potential $\psi_m + \psi_c$ as shaded contours in Figure 11.

Appendix B: Conductivity

In a homogeneous medium with no magnetic field, the relationship (Ohm's law) between the current density $\boldsymbol{J}$ and the rest-frame electric field $\boldsymbol{E}'$ is simply

$$\boldsymbol{J} = \sigma_0\ \boldsymbol{E}' \qquad \text{(B1)}$$

where the scalar quantity σ_0 is the conductivity of the medium. The electric field $\boldsymbol{E}'$ in our model consists of terms due to the magnetospheric potential and to the convective component $\boldsymbol{v}\times\boldsymbol{B}$.

If we now embed a magnetic field $\boldsymbol{B}$ in the medium, Ohm's law becomes dependent on the direction of the current and the scalar conductivity σ_0 is replaced by a tensor $\boldsymbol{\sigma}$, which is given in matrix form by

$$\boldsymbol{\sigma} = \begin{pmatrix} \sigma_1 & -\sigma_2 & 0 \\ \sigma_2 & \sigma_1 & 0 \\ 0 & 0 & \sigma_0 \end{pmatrix} \qquad \text{(B2)}$$

where the entries of the matrix are the direct (σ_0), Pedersen (σ_1) and Hall (σ_2) conductivities. The expression for $\boldsymbol{\sigma}$ given by (B2) is valid in any Cartesian coordinate system with z axis parallel to the direction of the magnetic field $\boldsymbol{B}$.

We now transform to a more general coordinate system, in which $\boldsymbol{B}$ has the components $\boldsymbol{B} = (B\cos i\cos\delta, -B\cos i\sin\delta, -B\sin i)$. In this form, B is the magnitude of the field, i is the magnetic dip angle, and δ is the magnetic declination angle. The latter two quantities may be angles measured in the conventional coordinate system used for global modeling, which is locally defined with the x axis pointing southwards, the y axis pointing east, and the z axis parallel to the local upward vertical. In this general coordinate system the conductivity tensor becomes

$$\boldsymbol{\sigma}' = (\sigma_0-\sigma_1)\cos i\times$$

$$\begin{pmatrix} \cos i\ \cos^2\delta & \cos i\ \sin\delta\ \cos\delta & -\sin i\ \cos\delta \\ \cos i\ \sin\delta\ \cos\delta & \cos i\ \sin^2\delta & -\sin i\ \sin\delta \\ -\sin i\ \cos\delta & -\sin i\ \sin\delta & \sin^2 i/\cos i \end{pmatrix}$$

$$+$$

$$\begin{pmatrix} \sigma_1 & \sigma_2\ \sin i & \sigma_2\ \cos i\ \sin\delta \\ -\sigma_2\ \sin i & \sigma_1 & -\sigma_2\ \cos i\ \cos\delta \\ -\sigma_2\ \cos i\ \sin\delta & \sigma_2\ \cos i\ \cos\delta & \sigma_1 \end{pmatrix} \qquad \text{(B3)}$$

The conductivity tensor $\boldsymbol{\sigma}'$ in equation (B3) is derivable from that of equation (B2) ($\boldsymbol{\sigma}$) by the relation $\boldsymbol{\sigma}' = \boldsymbol{R}\ \boldsymbol{\sigma}\ \boldsymbol{R}^{-1}$, where $\boldsymbol{R}$ is the matrix describing the transformation between the coordinate systems associated with each tensor. To calculate the horizontal current density, we used the condition of zero net vertical current ($J_z = 0$), corresponding to an isolated thermosphere [*Fuller-Rowell*, 1981]. This allows the vertical electric field to be determined, using the horizontal components (from $J_z = \sum_{i=1}^{3}\boldsymbol{\sigma}_{3i}E_i = 0$). The implied vertical current may then be computed (though not self-consistently) following the method of *Rees and Fuller-Rowell* [1989]. This assumes that the vertical currents flowing to and from the magnetosphere exactly match the horizontal currents in the ionosphere, such that the total divergence of current density van-

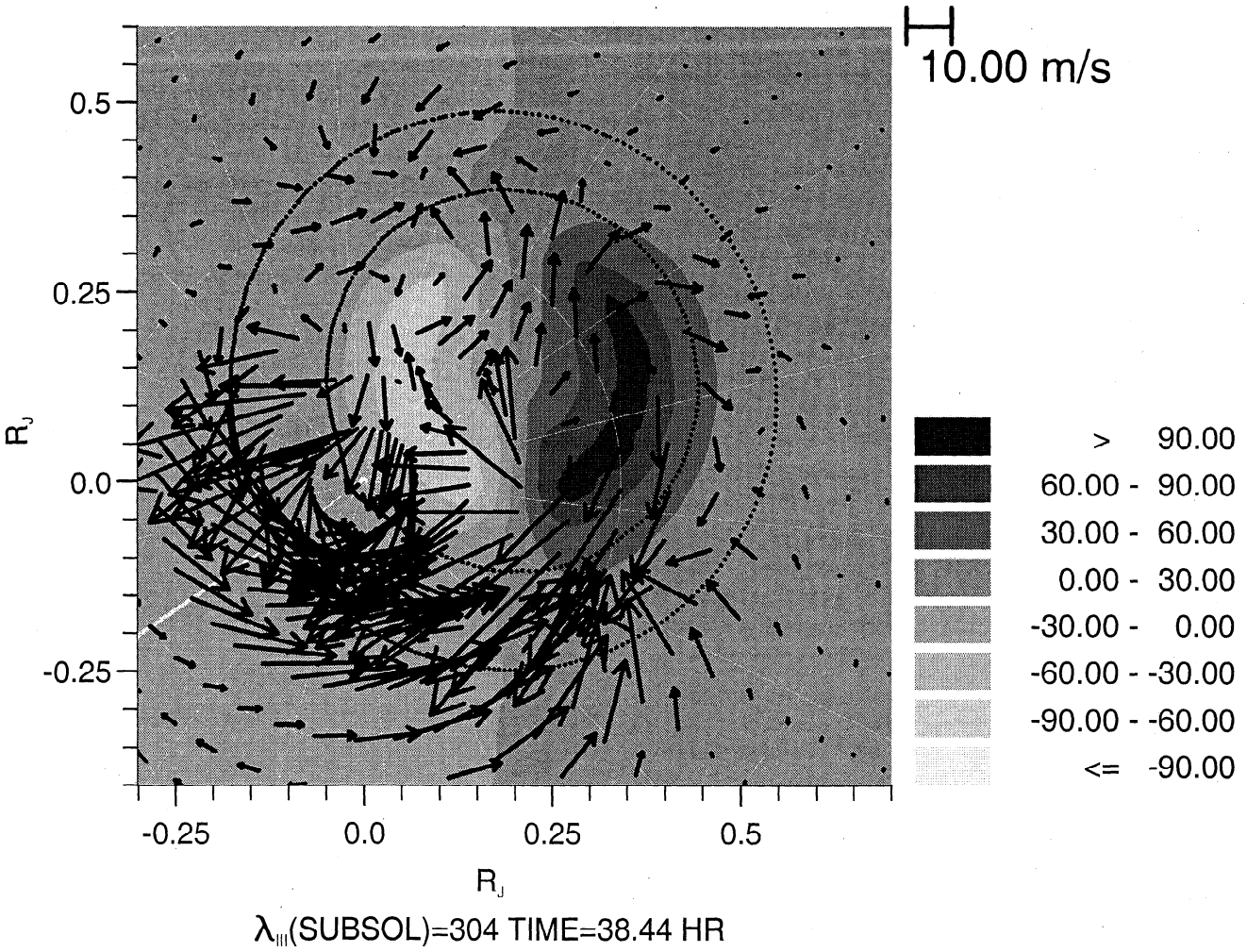

Figure 11. Electric potential and drift velocity. Contours of equal electric potential are shown for a northern polar region. The arrows show the distribution of horizontal electron drift velocity over the 1 nbar pressure level. The length of the arrows represents the magnitude of velocity, according to the scale bar shown. The local noon-midnight meridian is at $\lambda_{III} = 304°$ and is vertical in the figure. The bold meridian is at $\lambda_{III} = 0°$. The spacing for the longitude/latitude grid is 20°.

ishes ($\nabla \cdot \boldsymbol{J} = 0$). We show the horizontal electron drift velocity, computed from the electron contribution to $\boldsymbol{J}$, over the 1 nbar pressure level of the model in Figure 11.

Acknowledgments. N.A. wishes to acknowledge the support of a PPARC research grant and to thank the following people for their valuable assistance, advice, and patience: Gilda Ballester, Susan Branchett, Bianca Dinelli, Tim Fuller-Rowell, Kevin Hunter, Paul Lco, Liesl Neale, Renée Prangé, Daniel Rego, Pete Storey, and Hunter Waite.

References

Acuña, M. H., K. W. Behannon, and J. E. P. Connerney, Jupiter's magnetic field and magnetosphere, in *Physics of the Jovian Magnetosphere*, edited by A.J. Dessler, pp. 1–50, Cambridge Univ. Press, New York, 1983.

Atreya, S. K., *Atmospheres and Ionospheres of the Outer Planets and their Satellites*, Springer-Verlag, Heidelberg, 1986.

Atreya, S. K., and T. M. Donahue, Model ionospheres of Jupiter, in *Jupiter*, edited by T. Gehrels, pp. 304–318, Univ. of Ariz. Press, Tucson, 1976.

Atreya, S. K., T. M. Donahue, and M. C. Festou, Jupiter: Structure and composition of upper atmosphere, *Astrophys. J., 247*, L43–L47, 1981.

Atreya, S. K., T. M. Donahue, and J. H. Waite, An interpretation of the Voyager measurements of the Jovian electron density profiles, *Nature, 280*, 795–796, 1979.

Auerbach, D., R. Casak, R. Caudano, T. D. Gaily, C. J. Keyser, J. W. McGowan, J. B. A. Mitchell, and S. F. G. Wilk, Merged electron-ion beam experiments, I, Method and measurements of e-H_2^+ and e-H_3^+ dissociative recombination cross scctions, *J. Phys. B, 10*, 3797–3820, 1977.

Ballester, G. E., S. Miller, J. Tennyson, L. M. Trafton, and T. R. Geballe, Latitudinal temperature variations of jovian H_3^+, *Icarus, 107*, 189–194, 1994.

Ballester, G. E., et al., Time-resolved observations of Jupiter's far-ultraviolet aurora, *Science, 274*, 409–413, 1996.

Baron, R. L., T. Owen, J. E. P. Connerney, T. Satoh, and J. Harrington, Solar wind control of Jupiter's H_3^+ auroras, *Icarus, 120*, 437–442, 1996.

Clarke, J. T., et al., Far-ultraviolet imaging of Jupiter's aurora and the Io "footprint," *Science, 274*, 404–409, 1996.

Colegrove, F. D., F. S. Johnson, and W. B. Hanson, Atmospheric composition in the lower thermosphere, *J. Geophys. Res., 71*, 2227–2236, 1966.

Connerney, J. E. P., Magnetic fields of the outer planets, *J. Geophys. Res., 98*, 18,659–18,679, 1993.

Connerney, J. E. P., R. Baron, T. Satoh, and T. Owen, Images of excited H_3^+ at the foot of the Io flux tube in Jupiter's atmosphere, *Science, 262*, 1035–1038, 1993.

Connerney, J. E. P., T. Satoh, and R. L. Baron, Interpretation of auroral "lightcurves" with application to jovian H_3^+ emissions, *Icarus, 122*, 24–35, 1996.

Cook, G. R., and P. H. Metzger, Photoionization and absorption cross sections of H_2 and D_2 in the vacuum ultraviolet region, *J. Opt. Soc. Am., 54*, 968–972, 1964.

Cravens, T. E., Vibrationally excited molecular hydrogen in the upper atmosphere of Jupiter, *J. Geophys. Res., 92*, 11,083–11,100, 1987.

Danby, G., B. K. Elza, M. A. Morrison, and W. K. Trail, The separable representation of exchange in electron-molecule scattering, I, Elastic scattering and rotational excitation, *J. Phys. B, 29*, 2265–2287, 1996.

Datz, S., G. Sundstrom, C. Biedermann, L. Brostrom, H. Danared, S. Mannervik, J. R. Mowat, and M. Larsson, Branching processes in the dissociative recombination of H_3^+, *Phys. Rev. Lett., 74*, 896–899, 1995.

Drossart, P., B. Bézard, S. K. Atreya, J. Bishop, J. H. Waite Jr., and D. Boice, Thermal profiles in the auroral regions of Jupiter, *J. Geophys. Res., 98*, 18,803–18,811, 1993.

Drossart, P., et al., Detection of H_3^+ on Jupiter, *Nature, 340*, 539–541, 1989.

Eshleman, V. R., et al., Radio science with Voyager at Jupiter: Preliminary profiles of the atmosphere and ionosphere, *Science, 204*, 976–978, 1979a.

Eshleman, et al., Radio science with Voyager at Jupiter: Initial Voyager 2 results and a Voyager 1 measure of the Io torus, *Science, 206*, 959–962, 1979b.

Fjeldbo, G., A. Kliore, B. Seidel, D. Sweetnam, and D. Cain, The Pioneer 10 radio occultation measurements of the ionosphere of Jupiter, *Astron. Astrophys., 39*, 91–96, 1975.

Fjeldbo, G., A. Kliore, B. Seidel, D. Sweetnam, and P. Woiceshyn, The Pioneer 11 radio occultation measurements of the ionosphere of Jupiter, in *Jupiter*, edited by T. Gehrels, pp. 239–246, Univ. of Ariz. Press, Tucson, 1976.

Fuller-Rowell, T. J., A three-dimensional, time-dependent, global model of the thermosphere, Ph.D. Thesis, Univ. College London, 1981.

Fuller-Rowell, T. J., A two-dimensional, high-resolution, nested-grid model of the thermosphere, I, Neutral response to an electric field "spike," *J. Geophys. Res., 89*, 2971–2990, 1984.

Fuller-Rowell, T. J., and D. Rees, A three-dimensional, time-dependent, global model of the thermosphere, *J. Atmos. Sci., 37*, 2545–2567, 1980.

Fuller-Rowell, T. J., D. Rees, S. Quegan, R. J. Moffett, M. V. Codrescu, and G. H. Millward, A coupled thermosphere-ionosphere model (CTIM), in *Solar Terrestrial Energy Program (STEP) Handbook*, edited by R. W. Schulz, pp. 217–238, SCOSTEP, Boulder, 1996.

Geiss, J., and A. Bürgi, Diffusion and thermal diffusion in partially ionized gases in the atmospheres of the Sun and planets, *Astron. Astrophys., 159*, 1–15, 1986.

Gérard, J.-C., et al., A remarkable auroral event on Jupiter observed in the ultraviolet with the Hubble Space Telescope, *Science, 266*, 1675, 1994.

Gingerich, O., Review of opacity calculations, Proceedings: First Harvard-Smithsonian Conference on Stellar Atmospheres, *Smithson. Astrophys. Observ. Spec. Rep., 167*, 17–41, 1964.

Gingerich, O. (Ed.), *Theory and Observation of Normal Stellar Atmospheres*, p. 399, MIT Press, Cambridge, Mass., 1969.

Green, A. E. S., and T. Sawada, Ionization cross sections and secondary electron distributions, *J. Atmos. Terr. Phys., 34*, 1719–1728, 1972.

Heroux, L., and H. E. Hinteregger, Aeronomical reference spectrum for solar UV below 2000 Å, *J. Geophys. Res., 83*, 5305–5308, 1978.

Hinson, D. P., F. M. Flasar, A. J. Kliore, P. J. Schinder, J. D. Twicken and R. G. Herrera, Jupiter's ionosphere: results from the first Galileo radio occultation experiment, *Geophys. Res. Lett., 24*, 2107–2110, 1997.

Kim, Y. H., J. L. Fox, and H. S. Porter, Densities and vibrational distribution of H_3^+ in the jovian auroral ionosphere, *J. Geophys. Res., 97*, 6093–6101, 1992.

Lam, H. A., N. Achilleos, S. Miller, and J. Tennyson, A baseline spectroscopic study of the infrared auroras of Jupiter, *Icarus, 127*, 379–393, 1997.

Leu, M. T., M. A. Biondi, and R. Johnsen, Measurements of recombination of electrons with H_3^+ and H_5^+, *Phys. Rev. A., 8*, 413–419, 1973.

Lide, D. R. (Ed.), *CRC Handbook of Chemistry and Physics: 78th Edition*, CRC Press, Boca Raton, Fla., 1997.

Liu, W., and A. Dalgarno, The ultraviolet spectrum of the jovian dayglow, *Astrophys. J., 462*, 502–518, 1996.

Livengood, T. A., H. W. Moos, G. E. Ballester, and R. M. Prangé, Jovian ultraviolet auroral activity 1981–1991, *Icarus, 97*, 26–45, 1992.

Majeed, T., and J. C. McConnell, The upper ionospheres of Jupiter and Saturn, *Planet. Space Sci., 39*, 1715–1732, 1991.

Mason, E. A., and T. R. Marrero, The diffusion of atoms and molecules, *Adv. Mol. Phys., 6*, 156–232, 1970.

McConnell, J. C., and T. Majeed, H_3^+ in the Jovian ionosphere, *J. Geophys. Res., 92*, 8570–8578, 1987.

Miller, S., N. Achilleos, G. E. Ballester, H. A. Lam, J. Tennyson, T. R. Geballe, and L. M. Trafton, Mid-to-low latitude H_3^+ emission from Jupiter, *Icarus, 130*, 57–67, 1997.

Mitchell, J. B. A., The dissociative recombination of molecular ions, *Phys. Rep., 186*, 215–248, 1990.

Mitchell, J. B. A., C. T. Ng, D. P. Levac, R. E. Mitchell, P. M. Mul, W. Claeys, A. Sen, and J. W. McGowan, Measurement of the branching ratio for the dissociative recombination of $H_3^+ + e$, *Phys. Rev. Lett., 51*, 885–888, 1983.

Nagy, A. F., and P. M. Banks, Photoelectron fluxes in the ionosphere, *J. Geophys. Res., 75*, 6260–6270, 1970.

Olivero, J. J., J. N. Bass, and A. E. S. Green, Photoelectron excitation of the Jupiter dayglow, *J. Geophys. Res., 78*, 2812–2826, 1973.

Peart, B., and K. T. Dolder, Collisions between electrons and H_2^+ ions, II, Measurements of cross sections for dissociative excitation, *J. Phys. B, 5*, 860–865, 1972.

Peart, B., and K. T. Dolder, The production of de-excited H_3^+ ions and measurements of the energies of two electronically-excited states, *J. Phys. B, 7*, 1567–1573, 1974.

Porter, H. S., F. Varosi, and H. G. Mayr, Iterative solution of the multistream electron transport equation, 1, Comparison with laboratory beam injection experiments, *J. Geophys. Res., 92*, 5933–5959, 1987.

Prangé, R., The UV and IR jovian aurorae, *Adv. Space Res., 12*, 379–389, 1992.

Prangé, R., and M. Elkhamsi, Modeling the precipitation flux in the Jovian auroral zones 1, *J. Geophys. Res., 96*, 21,371–21,389, 1991.

Prangé, R., D. Rego, D. Southwood, P. Zarka, S. Miller, and W. Ip, Rapid energy dissipation and variability of the Io-Jupiter electrodynamic circuit, *Nature, 379*, 323–325, 1996.

Quegan, S., G. J. Bailey, R. J. Moffett, R. A. Heelis, T. J. Fuller-Rowell, D. Rees, and R. W. Spiro, Theoretical study of the distribution of ionization in the high-latitude

ionosphere and the plasmasphere: First results on the mid-latitude trough and the light-ion trough, *J. Atmos. Terr. Phys., 44*, 619–640, 1982.

Quegan, S., G. J. Bailey, R. J. Moffett, and L. C. Wilkinson, Universal Time effects on the plasma convection in the geomagnetic frame, *J. Atmos. Terr. Phys., 48*, 25–40, 1986.

Rees, D., and T. J. Fuller-Rowell, The response of the thermosphere and ionosphere to magnetospheric forcing, *Philos. Trans. R. Soc. London, Ser. A, 328*, 139–171, 1989.

Rego, D., R. Prangé, and J.-C. Gérard, Auroral Lyman alpha and H_2 bands from the giant planets, I, Excitation by proton precipitation in the jovian atmosphere, *J. Geophys. Res., 99*, 17,075–17,094, 1994.

Satoh, T., J. E. P. Connerney, and R. L. Baron, Emission source model of Jupiter's H_3^+ aurorae: A generalized inverse analysis of images, *Icarus, 122*, 1–23, 1996.

Seiff, A., D. B. Kirk, T. C. D. Knight, L. A. Young, F. S. Milos, E. Venkatapathy, J. D. Mihalov, R. C. Blanshard, R. E. Young, and G. Schubert, Thermal structure of Jupiter's upper atmosphere derived from the Galileo Probe, *Science, 276*, 102-104, 1997.

Shapiro, R., Smoothing, filtering and boundary effects, *Rev. Geophys., 8*, 359–387, 1970.

Shemansky, D. E., An explanation of the H Lyman-α longitudinal asymmetry in the equatorial spectrum of Jupiter, *J. Geophys. Res., 90*, 2673–2694, 1985.

Shemansky, D. E., J. M. Ajello, and D. T. Hall, Electron impact excitation of H_2, *Astrophys. J., 296*, 765–773, 1985.

Sommeria, J., L. Ben Jaffel, and R. Prangé, On the existence of supersonic jets in the upper atmosphere of Jupiter, *Icarus, 119*, 159–179, 1995.

Spiro, R. W., R. A. Heelis, and W. B. Hanson, Ion convection and the formation of the mid-latitude F region ionization trough, *J. Geophys. Res., 83*, 4255-4264, 1978.

Storey, P. J., and D. G. Hummer, Recombination line intensities for hydrogenic ions IV, *Mon. Not. R. Astron. Soc., 272*, 41–48, 1995.

Strobel, D., and S. Atreya, Ionosphere, in *Physics of the Jovian Magnetosphere*, edited by A.J. Dessler, pp. 51–67, Cambridge Univ. Press, New York, 1983.

Tawara, H., Y. Itikawa, H. Nishimura, and M. Yoshino, Cross sections and related data for electron collisions with hydrogen molecules and molecular ions, *J. Phys. Chem. Ref. Data, 19*, 617–636, 1990.

Theard, L. P., and W. T. Huntress Jr., Ion molecule reactions and vibrational deactivation of H_2^+ ions in mixtures of hydrogen and helium, *J. Chem. Phys., 60*, 2840–2848, 1974.

Trafton, L. M., J.-C. Gérard, G. Munhoven, and J. H. Waite Jr., High-resolution spectra of Jupiter's northern auroral ultraviolet emission with the Hubble Space Telescope, *Astrophys. J., 421*, 816–827, 1994.

Trafton, L., D. F. Lester, and K. L. Thompson, Unidentified emission lines in Jupiter's northern and southern 2 micron aurorae, *Astrophys. J., 343*, L73–L76, 1989.

Waite, J. H., Jr., T. E. Cravens, J. Kozyra, A. F. Nagy, S. K. Atreya, and R. H. Chen, Electron precipitation and related aeronomy of the Jovian thermosphere and ionosphere, *J. Geophys. Res., 88*, 6143–6163, 1983.

Waite, J. H., Jr., G. R. Gladstone, W. S. Lewis, P. Drossart, T. E. Cravens, A. N. Maurellis, B. H. Maulk, and S. Miller, Equatorial X-ray emissions: Implications for Jupiter's high exospheric temperatures, *Science, 276*, 104–108, 1997.

Yelle, R. V., H_2 emissions from the outer planets, *Geophys. Res. Lett., 15*, 1145–1148, 1988.

Young, L. A., R. V. Yelle, R. Young, A. Seiff, and D. Kirk, Gravity waves in Jupiter's thermosphere, *Science, 276*, 108–111, 1997.

N. Achilleos, S. Miller, and J. Tennyson, Department of Physics and Astronomy, University College London, Gower St, London WC1E 6BT, England. (e-mail: na@star.ucl.ac.uk; s.miller@ucl.ac.uk; j.tennyson@ucl.ac.uk)

A. D. Aylward and I. Mueller-Wodarg, Atmospheric Physics Laboratory, University College London, Gower St, London WC1E 6BT, England. (e-mail: alan@apg.ph.ucl.ac.uk; ingo@apg.ph.ucl.ac.uk)

D. Rees, Center for Atmospheric and Space Sciences, Utah State University, Logan, UT 84322-4405.

(Received November 26, 1997; revised February 26, 1998; accepted March 12, 1998.)